A&A 408, 621–649 (2003)
DOI: 10.1051/0004-6361:20030863

Astronomy & Astrophysics

Non-spherical core collapse supernovae

I. Neutrino-driven convection, Rayleigh-Taylor instabilities, and the formation and propagation of metal clumps

K. Kifonidis[1], T. Plewa[1–3], H.-Th. Janka[1], and E. Müller[1]

[1] Max-Planck-Institut für Astrophysik, Karl-Schwarzschild-Straße 1, 85741 Garching, Germany
[2] Nicolaus Copernicus Astronomical Center, Bartycka 18, 00716 Warsaw, Poland
[3] Center for Astrophysical Thermonuclear Flashes, University of Chicago, 5640 S. Ellis Avenue, Chicago, IL 60637, USA

Received 11 February 2003 / Accepted 28 May 2003

Abstract. We have performed two-dimensional simulations of core collapse supernovae that encompass shock revival by neutrino heating, neutrino-driven convection, explosive nucleosynthesis, the growth of Rayleigh-Taylor instabilities, and the propagation of newly formed metal clumps through the exploding star. A simulation of a type II explosion in a 15 $M_\odot$ blue supergiant progenitor is presented, that confirms our earlier type II models and extends their validity to times as late as 5.5 hours after core bounce. We also study a type Ib-like explosion, by simply removing the hydrogen envelope of the progenitor model. This allows for a first comparison of type II and type Ib evolution. We present evidence that the hydrodynamics of core collapse supernovae beyond shock revival differs markedly from the results of simulations that have followed the Rayleigh-Taylor mixing starting from ad hoc energy deposition schemes to initiate the explosion. We find iron group elements to be synthesized in an anisotropic, dense, low-entropy shell that expands with velocities of ~17 000 km s^{-1} shortly after shock revival. The growth of Rayleigh-Taylor instabilities at the Si/O and (C+O)/He composition interfaces of the progenitor, seeded by the flow-structures resulting from neutrino-driven convection, leads to a fragmentation of this shell into metal-rich "clumps". This fragmentation starts already ~20 s after core bounce and is complete within the first few minutes of the explosion. During this time the clumps are slowed down by drag, and by the positive pressure gradient in the unstable layers. However, at $t \approx 300$ s they decouple from the flow and start to propagate ballistically and subsonically through the He core, with the maximum velocities of metals remaining constant at ~3500–5500 km s^{-1}. This early "clump decoupling" leads to significantly higher ^{56}Ni velocities at $t = 300$ s than in one-dimensional models of the explosion, demonstrating that multi-dimensional effects which are at work within the first minutes, and which have been neglected in previous studies (especially in those which dealt with the mixing in type II supernovae), are crucial. Despite comparably high initial maximum nickel velocities in both our type II and our type Ib-like model, we find that there are large differences in the final maximum nickel velocities between both cases. In the "type Ib" model the maximum velocities of metals remain frozen in at ~3500–5500 km s^{-1} for $t \geq 300$ s, while in the type II model they drop significantly for $t > 1500$ s. In the latter case, the massive hydrogen envelope of the progenitor forces the supernova shock to slow down strongly, leaving behind a reverse shock and a dense helium shell (or "wall") below the He/H interface. After penetrating into this dense material the metal-rich clumps possess supersonic speeds, before they are slowed down by drag forces to ~1200 km s^{-1} at a time of 20 000 s post-bounce. While, due to this deceleration, the maximum velocities of iron-group elements in SN 1987 A cannot be reproduced in case of the considered 15 $M_\odot$ progenitor, the "type Ib" model is in fairly good agreement with observed clump velocities and the amount of mixing inferred for type Ib supernovae. Thus it appears promising for calculations of synthetic spectra and light curves. Furthermore, our simulations indicate that for type Ib explosions the pattern of clump formation in the ejecta is correlated with the structure of the convective pattern prevailing during the shock-revival phase. This might be used to deduce observational constraints for the dynamics during this early phase of the evolution, and the role of neutrino heating in initiating the explosion.

Key words. hydrodynamics – instabilities – nuclear reactions, nucleosynthesis abundances – shock waves – stars: supernovae: general

1. Introduction

The strong shock wave that has torn apart Sk –69° 202 and in consequence has given rise to Supernova SN 1987 A in the Large Magellanic Cloud on February 23rd, 1987, has also shattered the at that time widely shared belief that supernova explosions are essentially spherically symmetric events. The avalanche of observational data obtained since then from SN 1987 A has unambiguously demonstrated that the envelope of the progenitor star had substantially fragmented during

Send offprint requests to: K. Kifonidis,
e-mail: kok@mpa-garching.mpg.de

the explosion. Fast clumps of ^{56}Ni and its decay products had formed in the innermost regions of the ejecta and propagated out to the outer layers of the hydrogen envelope (i.e. close to the supernova's photosphere) within only *days* after core collapse (compare e.g. Mitchell et al. 2001). For a bibliography of the observational evidence see the reviews of Hillebrandt & Höflich (1989), Arnett et al. (1989a), McCray (1993), Nomoto et al. (1994), Wooden (1997), Müller (1998), and the references therein.

Spherical symmetry is not only broken in the case of SN 1987 A. This is apparently a generic feature, as is indicated by the spectra of a number of core collapse SNe that have been observed for more than one decade. Significant mixing and clumpiness of the ejecta were found for the type II explosions SN 1995 V (Fassia et al. 1998), SN 1988 A (Spyromilio 1991) and SN 1993 J (Spyromilio 1994; Wang & Hu 1994; Woosley et al. 1994). In case of type Ib supernovae the indications for mixing are even older. For instance, Filippenko & Sargent (1989) using [O I] observations have found that the ejecta of SN 1987 F were clumped. Even earlier, Harkness et al. (1987) in constructing synthetic spectra encountered the first evidence. They had to overpopulate excited states of He I by factors of $\sim 10^4$ relative to local thermodynamic equilibrium (LTE) conditions in order to reproduce the characteristic strong He lines of this supernova type. It was shown later by Lucy (1991) and Swartz et al. (1993) that the presence of the He I lines and the implied departures from LTE can be understood in terms of impact excitations and ionizations by nonthermal electrons. The latter are presumed to originate from Compton-scattering of the γ-rays from ^{56}Co decay and hence this hints toward significant outward mixing of ^{56}Co. Artificially mixed one-dimensional explosion models of type Ib progenitors indeed yield good fits to observed type Ib spectra and light curves (Woosley & Eastman 1997; Shigeyama et al. 1990).

Such observations have stimulated theoretical and numerical work on hydrodynamic instabilities, which up to now has been dichotomized into two distinct classes. On the one hand multi-dimensional modelling of the explosion mechanism was attempted (Herant et al. 1992; Burrows & Fryxell 1993; Miller et al. 1993; Herant et al. 1994; Burrows et al. 1995; Janka & Müller 1996; Mezzacappa et al. 1998), mainly with the aim to answer the question as to which extent convective instabilities are helpful for generating neutrino-driven explosions. Therefore, these simulations have been constrained to the early shock propagation phase up to about one second after core bounce.

In contrast, hydrodynamic models of the late-time shock propagation and the associated formation of Rayleigh-Taylor instabilities in the expanding mantle and envelope of the exploding star (Arnett et al. 1989b; Fryxell et al. 1991; Müller et al. 1991b,a,c; Hachisu et al. 1990, 1991, 1992, 1994; Yamada & Sato 1990, 1991; Herant & Benz 1991; Herant & Benz 1992; Herant & Woosley 1994; Shigeyama et al. 1996; Iwamoto et al. 1997; Nagataki et al. 1998; Kane et al. 2000) have ignored the complications of the explosion mechanism. Due to considerable computational difficulties in resolving the relevant spatial and temporal scales *all* of these latter investigations relied on ad hoc procedures to initiate the explosion. This usually meant that some simple form of energy deposition (by a piston or "thermal bomb") was used to generate a shock wave in a progenitor model. The subsequent propagation of the blast wave was followed in a one-dimensional simulation until the shock had reached the (C+O)/He or the He/H interface. Then, the 1D model was mapped to a multi-dimensional grid, and an assumed spectrum of seed perturbations was added to the radial velocity field in order to break the spherical symmetry of the problem and to trigger the growth of the instability. The studies of Yamada & Sato (1990, 1991), Nagataki et al. (1997, 1998), and the recent 3D calculations of Hungerford et al. (2003), who investigated the effects of metal mixing on X-ray and γ-ray spectra formation, differ from this universally adopted approach by making use of parameterized, aspherical shock waves.

All Rayleigh-Taylor calculations, that have been carried out to date for reproducing the mixing in SN 1987 A, share the same problem: With at most 2000 km s^{-1} their maximum ^{56}Ni velocities are significantly smaller than the observed values of 3500−4000 km s^{-1}. Herant & Benz (1992) dubbed this problem the "nickel discrepancy". They also speculated that it should disappear when the "premixing" of the ejecta during the phase of neutrino-driven convection is taken into account. On the other hand Nagataki et al. (1998) do not agree with Herant & Benz. They claim that the nickel discrepancy is resolved if the supernova shock is (mildly) aspherical. Similar conclusions have been reached by Hungerford et al. (2003). While Nagataki et al. as well as Hungerford et al. do not rule out neutrino emission from the neutron star as an explanation for the assumed asphericity of their shocks, Khokhlov et al. (1999), Wheeler et al. (2002) and Wang et al. (2002) questioned the neutrino-driven mechanism. Instead, they speculated on "jet-driven" explosions, which might originate from magneto-hydrodynamic effects in connection with a rapidly rotating neutron star.

The above controversy demonstrates the need for models which link observable features at very large radii to the actual energy source and the mechanism of the explosion. Without such models, interpretation of observational data requires caution. With the present work, which is the first in a series of papers on non-spherical core collapse supernova evolution, we attempt to provide this link for the standard paradigm of neutrino-driven supernovae. We have performed the first one and two-dimensional hydrodynamic calculations of type II and type Ib-like explosions of blue supergiant stars that reach from 20 ms up to 20 000 s (i.e. 5.5 hrs) after core bounce. Thus, we follow the evolution well beyond the time of shock eruption from the stellar photosphere. Our models include a detailed treatment of shock revival by neutrinos, the accompanying convection and nucleosynthesis and the growth of Rayleigh-Taylor instabilities at the composition interfaces of the progenitor star after shock passage. We employ high spatial resolution, which is mandatory to follow the episodes of clump formation, mixing, and clump propagation, by making use of adaptive mesh refinement techniques. Preliminary results of this work, which covered the first five minutes in the evolution of a type II supernova, were reported by Kifonidis et al. (2000).

This paper is organized as follows: we start with an account of the physical assumptions and numerical methods

implemented in our computer codes in Sect. 2. We then describe our stellar model in Sect. 3. Our boundary conditions along with some technical details of our computational strategy are discussed in Sect. 4. This is then followed in Sect. 5 with our description of the early evolution up to 0.82 s after core bounce. To focus the discussion, we restrict ourselves to one basic shock-revival model, from which we start all subsequent calculations. To illustrate its physics as clearly as possible, we first present the one-dimensional case in Sect. 5.1 and then the two-dimensional results in Sect. 5.2. In the same manner we discuss the subsequent evolution of a type II supernova model in Sect. 6. In Sect. 7, we consider the problem of a type Ib explosion by simply removing the hydrogen envelope of our progenitor. Section 8 finally contains our conclusions.

2. The codes

There is as yet no numerical code that could satisfactorily handle all the computational difficulties encountered in the modelling of core collapse supernovae over the time scales that we are interested in in this paper. Fortunately, however, such a code is not mandatory for studying the effects that are responsible for the formation and propagation of the nickel clumps. A crucial simplification arises from the fact that the physical character of the explosion changes fundamentally from a neutrino-hydrodynamic to a purely hydrodynamic problem once the shock has been revived and launched successfully by neutrino heating. A simulation of the long-time evolution of the ejecta can therefore be split into two parts. A neutrino-hydrodynamic calculation that encompasses the challenges of modelling neutrino-driven explosions but does not require an extremely high dynamical range of the spatial resolution, since only the innermost stellar core needs to be resolved adequately. In contrast, in the second, hydrodynamic part, the physics of the problem simplifies to the solution of the hydrodynamic equations because (to a good approximation) the central neutron star influences the dynamics of the ejecta only via its gravitational attraction and can otherwise be disregarded. It is this part of the calculation, however, where a high spatial resolution is essential in order to resolve the growth and expansion of Rayleigh-Taylor instabilities.

The separation into two largely independent problems might not be appropriate, if one is interested in an accurate determination of quantities that are influenced by the long-time hydrodynamic evolution of the layers near the neutron star. Among these quantities are the yields of *r*-process elements and the amount of fallback, which depend on the properties of the neutrino-driven wind as well as on the propagation of reverse shocks through the inner ejecta. We will not address these problems in the present work. Instead, we have developed two different codes to solve each of the sub-tasks described above: a modified version of the hydrodynamics code of Janka & Müller (1996) (henceforth JM96) that includes neutrino effects, and the adaptive mesh refinement (AMR) code AMRA, a FORTRAN implementation of the AMR algorithm of Berger & Colella (1989). Here we discuss only the most important features of these codes and give some details of our hydrodynamic advection scheme. AMRA is described in length in Plewa & Müller (2001).

Our goal is to study the main observational consequences of hydrodynamic instabilities in different layers of a supernova. We do not attempt to compete with the contemporary, highly sophisticated modelling of neutrino-driven explosions (for which an accurate treatment of neutrino transport is indispensable). For our purpose, a simple neutrino light-bulb algorithm, as the one of JM96, has the advantage to save enormous amounts of computer time as compared to detailled transport codes (see Rampp & Janka 2002, and the references therein). Omitting the core of the neutron star and replacing it by a boundary condition, that parameterizes its contraction and the radiated neutrino luminosities and spectra, we make use of the freedom to vary the neutrino properties. Thus we are able to control the explosion time scale and the final explosion energy in our simulations. By computing models with different values of the parameters, we can explore the physical possibilities as a consequence of neutrino-driven explosions. The local effects of neutrino heating and cooling by all relevant processes are treated reasonably well with our light-bulb scheme. However, a light-bulb description, of course, neglects all forms of back-reactions to the neutrino fluxes and spectra that result from neutrino absorption in the heating layer behind the supernova shock, and from neutrino emission associated with the accretion of matter onto the neutron star. We have recently developed a gray, characteristics-based scheme for the neutrino transport that accounts for spectral and luminosity modifications due to such effects. This new treatment is currently applied in new two and three-dimensional simulations. The calculations in this paper, however, were still performed with the light-bulb code.

The neutrino physics is combined with an enhanced version of the PPM hydrodynamics scheme (see below) and the equation of state (EOS) of JM96. The baryonic component of this EOS consists of 4 nuclei (neutrons, protons, α-particles and a representative nucleus of the iron group) in nuclear statistical equilibrium (NSE). These four species are also used to compute the energy source terms resulting from nuclear transmutations. In addition to this small NSE "network", but without feedback to the EOS and the hydrodynamics, we also evolve a 14 species nuclear reaction network to approximately calculate the products of explosive nucleosynthesis, whose spatial distribution we wish to follow. The latter network consists of the 13 α-nuclei from ^{4}He to ^{56}Ni and an additional tracer nucleus to which we channel the flow resulting from the reaction $^{52}\mathrm{Fe}(\alpha,\gamma)^{56}\mathrm{Ni}$ in case the electron fraction Y_e drops below 0.490 and ^{56}Ni ceases to be the dominant nucleus synthesized in the iron group (e.g. Thielemann et al. 1996). In this way we can "mark" material that freezes out from NSE at conditions of neutron excess and distinguish it from ^{56}Ni whose yield would otherwise be overestimated. The 14 species network is solved for temperatures between 10^8 K and 8×10^9 K. Above 8×10^9 K, we assume that nuclei have been disintegrated to α-particles. Of course, the 14 species network is a simplification of the nucleosynthesis processes in a supernova, since it neglects important isotopes and production channels of the considered nuclei. Moreover, in our current code version the heating and composition

changes due to explosive silicon, oxygen, neon, and carbon burning as described by the 14 species network are not taken into account in the solution of the hydrodynamics, which implies an approximation of the thermodynamical history of the regions where nuclear burning occurs. However, the hydrodynamic evolution should hardly be affected in the simulations presented in this paper. This can be seen by estimating the energy release due to nuclear transmutations. In core-collapse supernovae three thermodynamic regimes can be distinguished. Below 2.1×10^9 K (the minimum temperature required for explosive Ne/C burning; Thielemann et al. 1996) nuclear burning time scales are large compared to the hydrodynamic expansion time scale of the layers that contain the nuclear fuel, and no appreciable nucleosynthesis occurs. For temperatures 2.1×10^9 K $\leq T \leq 5 \times 10^9$ K the burning time scales are comparable to the expansion time scale, and the abundance and energy changes need to be followed by solving a nuclear reaction network. Above 5×10^9 K NSE holds, i.e. the composition adjusts immediately to temperature and density changes caused by the hydrodynamics. In our code, energy source terms due to explosive burning are not accounted for only in the second regime (in the NSE regime the energy source term is obtained from the 4 species network). For the 15 $M_\odot$ Woosley et al. (1988) progenitor that we employed (see Sect. 3), we estimated that thermonuclear burning in layers with temperatures 2.1×10^9 K $\leq T \leq 5 \times 10^9$ K releases $\sim 5 \times 10^{49}$ ergs. This energy is small compared to the explosion energies of our models (about 1.8×10^{51} ergs), and is therefore negligible with respect to the dynamics. This may not be true, however, in case of other (e.g. more massive) progenitors.

Gravity is taken into account in our neutrino-hydrodynamics code by solving Poisson's equation in two spatial dimensions with the algorithm of Müller & Steinmetz (1995). To avoid the formation of transient shock oscillations in case general relativistic post collapse models are used as initial data (compare JM96), we add 1D (i.e. spherical) general relativistic corrections to the 2D Newtonian gravitational potential as in Keil et al. (1996) (see Rampp & Janka 2002 for details of the implementation and compare also to van Riper 1979). These corrections are especially important in the early phase of shock revival, since the deeper relativistic potential well keeps the shock at significantly smaller radii than in the Newtonian case. However, Newtonian gravity becomes an excellent approximation at large distances from the neutron star. Therefore it can be used once the shock has emerged from the iron core and propagates through the oxygen shell. This is also the time when we map our explosion models to follow the late evolution with AMRA. In the AMR calculations Poisson's equation is solved in one spatial dimension with an angular average of the density. The equation of state that we employed for these simulations includes contributions from non-relativistic, non-degenerate electrons, photons, electron-positron pairs (the formulae for pressure and energy density due to pairs can be derived from information given by Witti et al. 1994) and the 14 nuclei (treated as Boltzmann gases) that are included in the reaction network of our neutrino code. Separate continuity equations are solved for each of these nuclei in order to determine the mixing of the elements.

The neutrino-hydrodynamics code as well as AMRA, make use of the HERAKLES hydrodynamics solver, an implementation of the direct Eulerian version of the Piecewise Parabolic Method (PPM) of Colella & Woodward (1984). HERAKLES originated from the PROMETHEUS code of Fryxell et al. (1991). It includes the entire functionality of PROMETHEUS, but differs from its predecessor in the following aspects. The handling of multifluid flows of Fryxell et al. (1991) is replaced by the Consistent Multifluid Advection scheme (CMA) of Plewa & Müller (1999). This allows for a significant reduction of numerical diffusion of nuclear species (to the level that is characteristic for the PPM advection scheme) without suffering from errors in local mass conservation (see Plewa & Müller 1999). Further improvements in reducing the numerical diffusivity of the code are achieved by adopting the elaborate procedure for the flattening of interpolated profiles for the (primitive) state variables that is suggested in the Appendix of Colella & Woodward (1984). Additionally, the algorithm for the computation of the left and right input states for the Riemann problem is revised. The version of HERAKLES that is used as hydrodynamic solver in our AMR calculations has been further extended to achieve good computational performance even on small grid patches. For this purpose a new memory interface was written, that allows for optimal pipelining of the one-dimensional hydrodynamic sweeps that result from dimensional splitting in multi-dimensional calculations, while due attention is paid to optimal cache reuse. With this memory interface the code can make efficient use of both superscalar as well as vector computer architectures.

The most important modifications as compared to PROMETHEUS (or other standard implementations of the PPM scheme) are, however, the inclusion of new algorithms for the artificial viscosity and for multi-dimensional shock detection, along with the addition of Einfeldt's HLLE Riemann solver (Einfeldt 1988). Following Quirk (1994, 1997) we use the Einfeldt solver for zones inside strong grid-aligned shocks, while we retain the (less diffusive) Riemann solver of Colella & Glaz (1985) for all remaining grid cells. The latter changes are necessary to eliminate the odd-even decoupling instability (Quirk 1994, 1997; Liou 2000), from which the original Colella & Glaz solver suffers (Kifonidis et al. 2000). This numerical failure shows up if a sufficiently strong shock is (nearly) aligned with one of the coordinate directions of the grid, and if, in addition, the flow is slightly perturbed. Many Riemann solvers allow these perturbations to grow without limit along the shock surface, thus triggering a strong rippling of the shock front and the post-shock state. In supernova simulations, these perturbations strongly enhance the growth of hydrodynamic instabilities, since their amplitudes can exceed those of the intentionally introduced seed perturbations by several orders of magnitude. In case of neutrino-driven convection this leads to faster growth of convective instabilities and angular wavelengths of convective bubbles which are significantly larger than in a "clean" calculation. This is demonstrated in Fig. 1 where we compare entropy plots of two simulations of neutrino-driven convection that were conducted using spherical coordinates and the neutrino parameters given in Sect. 5.1.

The first of these (Fig. 1a) was done with our original PROMETHEUS version and a resolution of 400×180 zones and is affected by odd-even decoupling, while the second (Fig. 1b) was obtained with the improved scheme implemented in HERAKLES using 400×192 zones.

Odd-even decoupling and the associated carbuncle phenomenon (i.e. a local occurrence of odd-even decoupling for shocks that are only partly aligned with the grid; Quirk 1994, 1997; LeVeque 1998) have gone largely unnoticed in the astrophysics literature and have marred almost all multi-dimensional supernova simulations conducted to date on cylindrical or spherical grids with hydrodynamic codes that are based on Riemann solver type schemes (e.g. Kifonidis et al. 2000; Mezzacappa et al. 1998; Iwamoto et al. 1997; Janka & Müller 1996; Burrows et al. 1995; Hachisu et al. 1994; Burrows & Fryxell 1993; Hachisu et al. 1992; Müller et al. 1991a).

3. The stellar model

As in JM96 and Kifonidis et al. (2000) the initial model adopted for our study originated from the simulations of Bruenn (1993), who followed core collapse and bounce of the $15\,M_\odot$ blue supergiant progenitor of Woosley et al. (1988). We have set up our shock revival calculations using his model WPE15 LS (180) at a time of 20 ms after core bounce. However, Bruenn's data set extends only to layers within the stellar He core and the original progenitor model of Woosley et al. (1988) is no longer available. To follow the late-time propagation of the shock in our subsequent AMR calculations we thus had to reconstruct the outer envelope of the Woosley et al. star. For this purpose we used a new $15\,M_\odot$ blue supergiant model (S. E. Woosley, private communication) that was smoothly joined to Bruenn's data by choosing a matching point at 8.4×10^9 cm ($M_\mathrm{r} = 1.94\,M_\odot$), i.e. within the He core. Table 1 summarizes the location of the composition interfaces and the initial position of the Y_e discontinuity (that defines the boundary of the iron core according to Woosley & Weaver 1995) of the resulting "hybrid" $15\,M_\odot$ progenitor. Except for the He/H interface, the listed radii were taken from the post-collapse data of Bruenn (1993).

Since the velocity of the supernova shock and the associated growth of Rayleigh-Taylor instabilities are very sensitive to the density profile, we have verified in a number of one-dimensional test calculations that the hybrid stellar model had no adverse effects on shock propagation. In these calculations we cut out the model's iron core and induced the explosion artificially by depositing $\sim 10^{51}$ ergs in the form of thermal energy at the inner boundary of the silicon shell. This procedure enabled us to compare the hydrodynamic evolution of our hybrid model with induced explosions of newer SN 1987 A progenitor models computed by Woosley et al. (1997) (for which no collapse calculations including neutrino transport were available at the time we performed our simulations). No differences pointing to numerical artifacts were found.

Table 1. Location of chemical interfaces in our progenitor model at 20 ms after core bounce.

	Y_e disc.	Fe/Si	Si/O	(C+O)/He	He/H
r [km]	260	1376	6043	29 800	708 000
M_r [$M_\odot$]	1.25	1.32	1.50	1.68	4.20

4. Computational setup

4.1. Explosion models (hydrodynamic calculations with neutrinos)

To set up a shock revival simulation we adopt spherical coordinates. We omit the innermost $0.848\,M_\odot$ of the core of the neutron star and replace it by the gravitational potential of a point mass and an inner boundary which acts as a neutrino source. This boundary is placed at a radius of 3.17×10^6 cm, which is somewhat below the electron neutrinosphere in Bruenn's model. The outer radial boundary is located at $r = 1.7 \times 10^9$ cm, inside the C+O-core of the star. Our grid consists of 400 non-equidistant radial zones that yield a maximum resolution of 1.2 km at the neutron star and 200 km at the outer grid boundary. In our two-dimensional models 192 angular zones are distributed uniformly between $0 \le \theta \le \pi$ and axial symmetry is assumed around the polar axis. Reflecting boundaries are imposed at $\theta = 0$ and $\theta = \pi$ and a random initial seed perturbation is added to the velocity field on the entire grid with a modulus of 10^{-3} of the (radial) velocity of the post-collapse model. In the immediate upstream region of the accretion shock, this corresponds to velocity perturbations with a modulus of $\sim 5 \times 10^{-3}$ of the local sound speed, while further outward this value decreases with the decreasing infall velocities to $\sim 10^{-3}$.

In order to mimic the contraction of the cooling and deleptonizing proto-neutron star, the inner boundary is moved inward during the computations, approximating the motion of the corresponding mass shell in Bruenn's calculations. This is achieved by making use of the moving grid implemented in our code (cf. JM96 for details). Free outflow is allowed for across the outer radial boundary. With this setup, the time-step resulting from the Courant-Friedrichs-Lewy stability condition is typically of the order of a few 10^{-5} s in one-dimensional calculations, and several 10^{-6} s in two-dimensional simulations. Starting at 20 ms after core bounce the computations are continued until 820 ms post-bounce, when the explosion energy has saturated and all nuclear reactions have frozen out.

4.2. Models for the Rayleigh-Taylor mixing (AMR calculations)

By performing test calculations we have found that, in order to enable a sufficiently detailed study of the growth of all relevant Rayleigh-Taylor instabilities, a spatial resolution of $\Delta r \le 10^{-6} R$ (with R being the stellar radius) is required for at least some fraction of the time that it takes the shock to erupt from the surface of the star. The above estimate holds for the case of a blue supergiant like Sk -69° 202. In case of a red supergiant an even smaller ratio $\Delta r / R$ would be necessary. Without adaptive mesh refinement and/or a moving grid

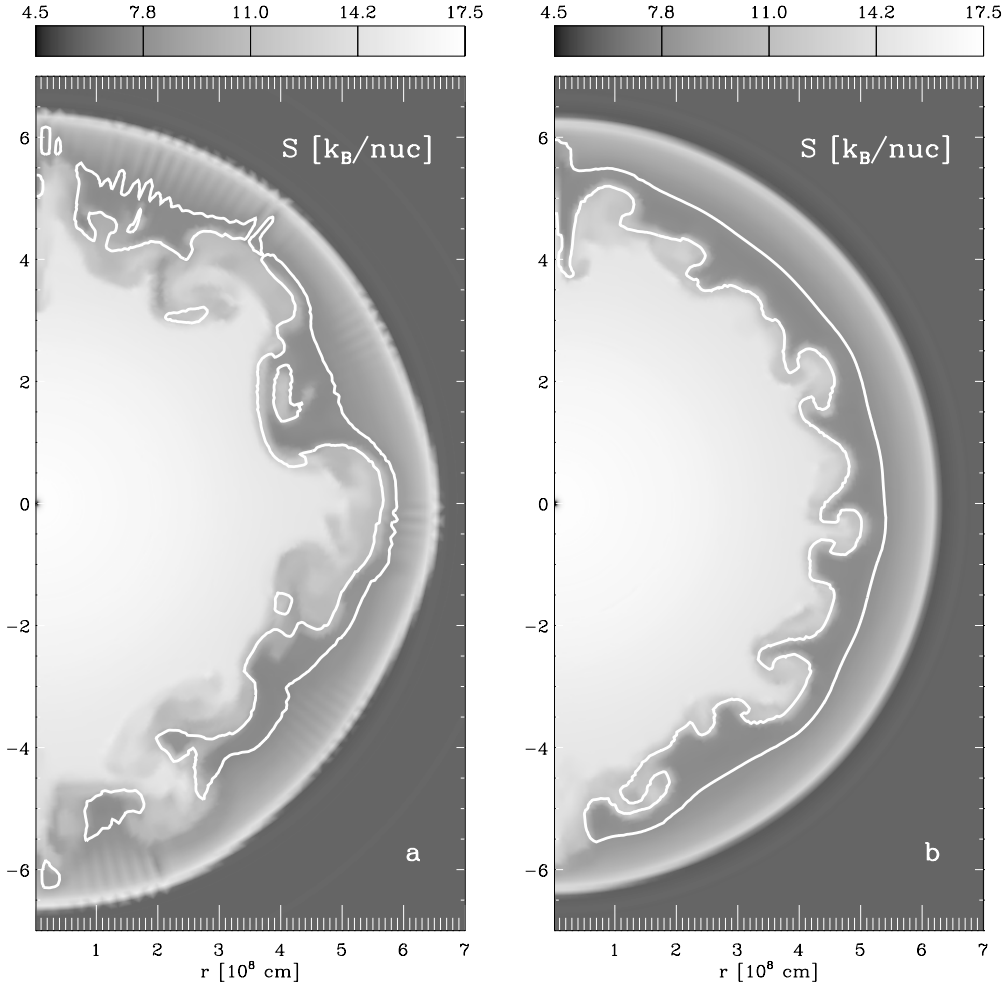

Fig. 1. Entropy (in units of k_B per nucleon) in Model T310 at a time of 420 ms after core bounce. The white contour line encloses the region where the ^{56}Ni mass fraction is ≥20%. **a)** Calculation performed with the original PROMETHEUS code showing odd-even decoupling. Note the deformation of the shock. **b)** Calculation performed with HERAKLES.

such calculations are currently unfeasible, especially in more than one spatial dimension. While this range of spatial scales appears formidable, for explicit codes like PPM an even more severe difficulty is posed by the vastly differing time scales involved in the problem. Even if the inner boundary is placed far away from the neutron star, and the gravitational attraction of the omitted stellar layers is taken into account by a point mass, the resulting Courant time step is still too small to allow one to follow the evolution over hours. The small time step is caused by fallback, which leads to high sound speeds in the central zones because matter that falls back toward the inner boundary is compressed and heated. The only remedies to this problem that we have found to be practical are either a coarsening of the grid or a shift of the inner boundary with time towards larger radii, where smaller temperatures are encountered. While the former is useful in 1D calculations, where the remaining grid resolution that we achieved was still reasonable (see below), the latter proved to be the better choice for our two-dimensional calculations.

In all of our AMR simulations we have adopted spherical coordinates and a pre-chosen AMR grid hierarchy to which we mapped the data of our explosion models *without adding any extra seed perturbations*. At radii where data from the explosion models are not available, the structural information is taken from the progenitor model. The inner regions of an explosion model are cut out by placing the inner boundary of the AMR base level grid at a radius of 10^8 cm, which is well inside the neutrino-driven wind of the neutron star. This baryonic mass flow is therefore neglected in the subsequent evolution. Instead we allowed for free outflow through the inner (as well as the outer) boundary. This is certainly a gross simplification for the evolution of the innermost regions of the flow during the first minute of the explosion (but becomes more realistic later when the neutrino wind is expected to cease). By ignoring the neutrino wind one obtains early fallback of matter through the inner boundary. In addition, the evolution of the reverse shock, which results from the slow-down of the main shock in the oxygen core, is affected. This reverse shock separates the wind from the outer ejecta at times later than ~500 ms after bounce (compare Sect. 5). Without the pressure of the wind, the reverse shock propagates inward and is (partially) reflected at the inner boundary because the latter is not perfectly transmitting for numerical reasons. Although both the inward motion and reflection of the reverse shock are expected to happen

once the wind weakens (with the reverse shock being reflected at the steep density gradient near the neutron star "surface"), our approximations do not allow to model these phenomena reliably in space and time. Except for resulting in these limitations (which are not relevant for studying clump formation and propagation), the mapping from one code to the other worked very well and did not produce any noticeable artifacts.

For our 1D AMR calculation of Sect. 6.1, we employed a grid hierarchy with a base grid resolution of 512 zones and 7 levels of refinement. We use two criteria to flag zones on a given level for refinement. First, we estimate the local truncation error for the (mass) density, momentum density, total energy density, and the partial densities of nuclei, ρX_i, using Richardson extrapolation. Whenever the error for one of these quantities is found to be $\geq 10^{-2}$ (or $\geq 10^{-3}$ in case of the ρX_i), we flag the corresponding zone for refinement. Independent of the truncation error estimate, we also flag zones in which density jumps ≥100% are encountered as compared to neighbouring zones. To refine between different levels, we use factors of 4 in resolution until level 5 is reached, where we switch to refinement factors of 2. With this scheme we achieve a maximum resolution equivalent to 524 288 equidistant zones. Since the outer boundary of the computational domain is kept at the stellar radius of 3.9×10^{12} cm, this translates to an absolute resolution of ∼75 km. Using this setup, we measure speed-up factors (as compared to using a uniform grid) that are as large as 10^3. Still, however, the small time step resulting from the high sound speed in the innermost zones leads to long computing times. We therefore remove the 7th level of the grid hierarchy after 1870 s of evolution and thereby reduce the maximum resolution to 149 km. This zoning is kept until $t = 4770$ s, when also level 6 is discarded and the rest of the evolution followed with a maximum resolution of 298 km. It should be noted that AMR allows one to introduce this coarsening in a rather straightforward fashion by manually resetting the refinement flags returned from the error estimation and zone flagging modules of the code. The grid can even be coarsened only locally if required. Our 1D simulation is stopped at $t = 8500$ s post bounce, 1700 s after the shock has emerged from the photosphere.

For our 2D calculations we have adopted a different approach, combining mesh refinement with a "zooming" algorithm for the radial coordinate. The AMR grid is chosen such that a base-level resolution of 48×12 zones and four levels of refinement with refinement factors of 4 in each dimension are employed. This results in a maximum resolution on the finest level corresponding to 3072 equidistant zones in radius and 768 zones in angle. Zones are flagged for refinement by applying the same criteria as in our one-dimensional calculation for each dimension. Adopting transmitting boundary conditions in the radial and reflecting boundaries in the angular direction, our computational volume is initially set up to span the domain $(1000 \leq r/\mathrm{km} \leq 48\,000) \times (0 \leq \theta \leq \pi)$. While the grid boundaries in θ direction are kept unchanged throughout the calculation, the zooming algorithm successively enlarges the radial extent of the grid according to Table 2, when the shock is approaching the outer grid boundary, r_{out}. Whenever it is time to regrid, we also move the inner grid boundary, r_{in}, away from the central remnant. This approach allows us to concentrate the computational effort in the post-shock and the Rayleigh-Taylor unstable regions while avoiding overly restrictive Courant time steps due to fallback. The times t_{i} and t_{f} over which the radial grid boundaries are kept fixed are given in columns one and two of Table 2. The "zooming algorithm" allows us to temporally achieve a radial resolution of $\Delta r = 15$ km in the unstable layers, that is equivalent to covering the entire star with an effective resolution of $N_{\mathrm{r}}^{\mathrm{eff}} = 2\,599\,933$ equidistant zones. Even with this combination of mesh refinement, grid enlargement and inner boundary movement, however, the computational load is still significant. The two-dimensional AMR calculation that we present in Sect. 6, and which follows the evolution of the mixing from 820 ms to 5.5 hrs after core bounce, requires nearly 2×10^{15} floating point operations (this number has to be multiplied by about a factor of 5 if no adaptive mesh is used).

Table 2. Computational setup for the 2D AMR calculation T310a. (see Sect. 6.2). The initial and final times over which the inner and outer grid boundaries were held fixed at r_{in} and r_{out}, are denoted by t_{i} and t_{f}, respectively. Δr is the (absolute) resolution and $N_{\mathrm{r}}^{\mathrm{eff}}$ the number of equidistant radial zones that would have been required to cover the entire star in order to achieve a resolution of Δr. Exponents are given in brackets.

t_{i} [s]	t_{f} [s]	r_{in} [cm]	r_{out} [cm]	Δr [km]	$N_{\mathrm{r}}^{\mathrm{eff}}$
0.8(+0)	2.3(+0)	1.0(+8)	4.8(+9)	1.5(+1)	2 599 933
2.3(+0)	8.0(+0)	1.7(+8)	1.4(+10)	4.6(+1)	847 804
8.0(+0)	3.4(+1)	3.9(+8)	4.3(+10)	1.4(+2)	280 568
3.4(+1)	1.2(+2)	9.9(+8)	1.3(+11)	4.2(+2)	93 299
1.2(+2)	2.8(+2)	2.3(+9)	2.6(+11)	8.4(+2)	46 650
2.8(+2)	6.5(+2)	3.9(+9)	5.2(+11)	1.7(+3)	23 282
6.5(+2)	1.5(+3)	6.8(+9)	1.0(+12)	3.4(+3)	11 634
1.5(+3)	3.6(+3)	1.2(+10)	2.1(+12)	6.7(+3)	5810
3.6(+3)	2.0(+4)	2.0(+10)	3.9(+12)	1.3(+4)	3072

Finally, we note that the choice of spherical coordinates leads to numerical artifacts along the symmetry axis of the grid. The excessive outflows that we observe for $\theta \approx 0$ and $\theta \approx \pi$ for the models in this paper are much weaker than those in Kifonidis et al. (2000). Nevertheless, in order to avoid spurious effects, we have excluded a cone with an opening angle of 15° around the polar axis for evaluating our simulations for the velocity distributions of nucleosynthesis products and the angle-averaged extent of the mixing of chemical elements.

5. The first second

5.1. Evolution in one dimension

In Table 3 we summarize the basic parameters of our one-dimensional explosion, Model O310, along with its two-dimensional counterpart, Model T310, that will be discussed in Sect. 5.2. As described in detail in JM96 the models are characterized by the initial values of the electron and heavy lepton neutrino luminosities (in units of 10^{52} erg/s), $L^0_{\nu_{\mathrm{e}},52}$ and $L^0_{\nu_x,52}$, and the energy loss (in units of $M_\odot c^2$) and lepton loss parameters of the inner iron core, $\Delta\varepsilon$ and ΔY_{L}, respectively. The latter parameter constrains the luminosity of electron antineutrinos

Table 3. Parameters of Models O310 and T310. The (baryonic) mass of the inner core, $M_{\rm core}$, that has been excluded from the simulation, and the final neutron star mass, $M_{\rm ns}$, are given in solar masses. The initial and final radius of the inner core, $R^0_{\rm core}$ and $R^\infty_{\rm core}$, respectively, are given in km, and its initial velocity of contraction, $\dot{R}^0_{\rm core}$, in km s^{-1}. The initial neutrino luminosities of different flavours, $L^0_{\nu_{\rm e},52}$, $L^0_{\bar{\nu}_{\rm e},52}$, and $L^0_{\nu_x,52}$ (see also the main text), are given in units of 10^{52} erg/s, and the energy loss of the inner core, $\Delta\varepsilon$, in units of $M_\odot c^2$. The explosion energy, $E_{\rm exp,51}$, and the explosion time scale, $t_{\rm exp}$, are given in 10^{51} erg and in ms, respectively.

Model	Resolution	$M_{\rm core}$	$R^0_{\rm core}$	$\dot{R}^0_{\rm core}$	$R^\infty_{\rm core}$	$L^0_{\nu_{\rm e},52}$	$L^0_{\bar{\nu}_{\rm e},52}$	$L^0_{\nu_x,52}$	$\Delta Y_{\rm L}$	$\Delta\varepsilon$	$E_{\rm exp,51}$	$t_{\rm exp}$	$M_{\rm ns}$
O310	400	0.848	31.7	50	18.1	3.094	3.684	2.613	0.0963	0.0688	1.59	70	1.12
T310	400×192	0.848	31.7	50	18.1	3.094	3.684	2.613	0.0963	0.0688	1.77	62	1.09

while $\Delta\varepsilon$ determines the characteristic time scale for the decay of the luminosities that we assume to follow the simple exponential law

$$L_{\nu_i} = L^0_{\nu_i} {\rm e}^{-t/t_{\rm L}}, (\nu_i \equiv \nu_{\rm e}, \bar{\nu}_{\rm e}, \nu_x) \quad (1)$$

where $t_{\rm L}$ is of the order of 700 ms. The neutrino spectra are prescribed in the same way as in JM96.

Table 3 also lists the explosion time scale, $t_{\rm exp}$, measured in ms and the explosion energy at the end of the shock-revival simulation, $E_{\rm exp,51}$, in units of 10^{51} erg (note that the binding energy of the envelope has not yet been subtracted from the latter). We define these quantities as in JM96. The explosion energy is given by the sum of the gravitational, kinetic and internal energy of all zones of the grid where this sum of energies is positive. The explosion time scale is defined as the time after the start of the simulation when the explosion energy exceeds 10^{48} erg.

We adopt values for $L^0_{\nu_{\rm e},52}$ and $L^0_{\nu_x,52}$ that give rise to energetic explosions. This choice was motivated by the claim of Herant & Benz (1992) that premixing of the ^{56}Ni (be it artificial or due to neutrino-driven convection) in models with high explosion energies of about 2×10^{51} ergs leads to a resolution of the "nickel discrepancy problem". In their simulations of Rayleigh-Taylor instabilities in the stellar envelope, they obtained final maximum ^{56}Ni velocities of up to 3000 km s^{-1} if they premixed the ^{56}Ni in their 1D initial models out to mass coordinates of 1.5 $M_\odot$ above the Fe/Si interface (i.e. throughout 75% of the metal core of the progenitor model of Nomoto et al. 1988).

With the parameters listed in Table 3, shock revival by neutrino heating is almost instant in our simulations. The shock shows neither long stagnation times nor phases of progression and subsequent recession. Instead, it moves out of the iron core without noticeable delay. To illustrate matters, we show a spacetime plot of the evolution of the density with time for Model O310 in Fig. 2, from which one can infer a mean shock velocity of about 19 000 km s^{-1} after 0.2 s. Additionally, in Fig. 3 we depict the evolution of the most important hydrodynamic and thermodynamic quantities as a function of radius. The initial post-collapse profiles are plotted with thick lines, and the Si/O interface can be discerned by the associated entropy step at $\log r$ [cm] = 8.8. One can easily recognize the transition of the accretion shock to an outward propagating shock with high post-shock velocities, the rarefaction generated by the explosion and the deleptonization and contraction of the outer layers of the proto-neutron star in response to the contracting inner boundary. Figure 3 also shows

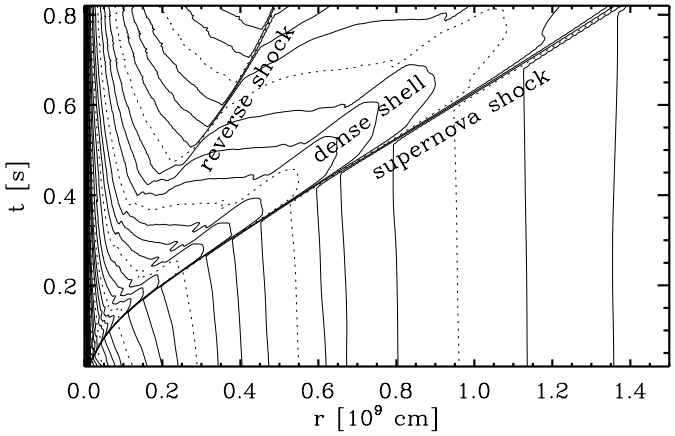

Fig. 2. Spacetime plot for the evolution of the logarithm of the density for our one-dimensional explosion, Model O310. The supernova shock is visible as the outermost discontinuity that extends diagonally through the plot. Around 500 ms a reverse shock forms in the inner ejecta that originates from the (hardly visible) slight deceleration of the main shock in the oxygen core. The reverse shock separates the ejecta from the neutrino-driven wind.

the neutrino-driven wind, that is blown off the surface of the neutron star for times later than ∼200 ms and that has also been found in the calculations of Burrows et al. (1995) and Janka & Müller (1996). Furthermore, a reverse shock is visible, that forms about 500 ms after core bounce (compare Fig. 2) when the main shock enters the oxygen core of the star and propagates into layers with a somewhat flatter density gradient, thereby decelerating slightly. Both shocks mark the boundaries of a dense region that contains most of the ejecta, while the reverse shock separates the ejecta from the neutrino-driven wind. Shortly after the supernova shock has crossed the Fe/Si interface at 120 ms (at this time the latter has fallen in from its initial radius of $r = 1.38\times10^8$ cm to 8×10^7 cm), a high-density shell forms immediately behind the shock. It becomes more pronounced after $t = 500$ ms when the shock has passed the Si/O interface. The trajectory of the shell's inner boundary can be discerned in Fig. 2 in between the supernova and reverse shocks. This shell is one of the most interesting outcomes of our calculations. Three important physical processes take place in this part of the ejecta, whose mutual interaction has been neglected in previous attempts to model supernova explosions. These processes are ^{56}Ni-synthesis, neutrino-driven convection, and the growth of Rayleigh-Taylor instabilities at the Si/O interface of the progenitor's metal core. We address

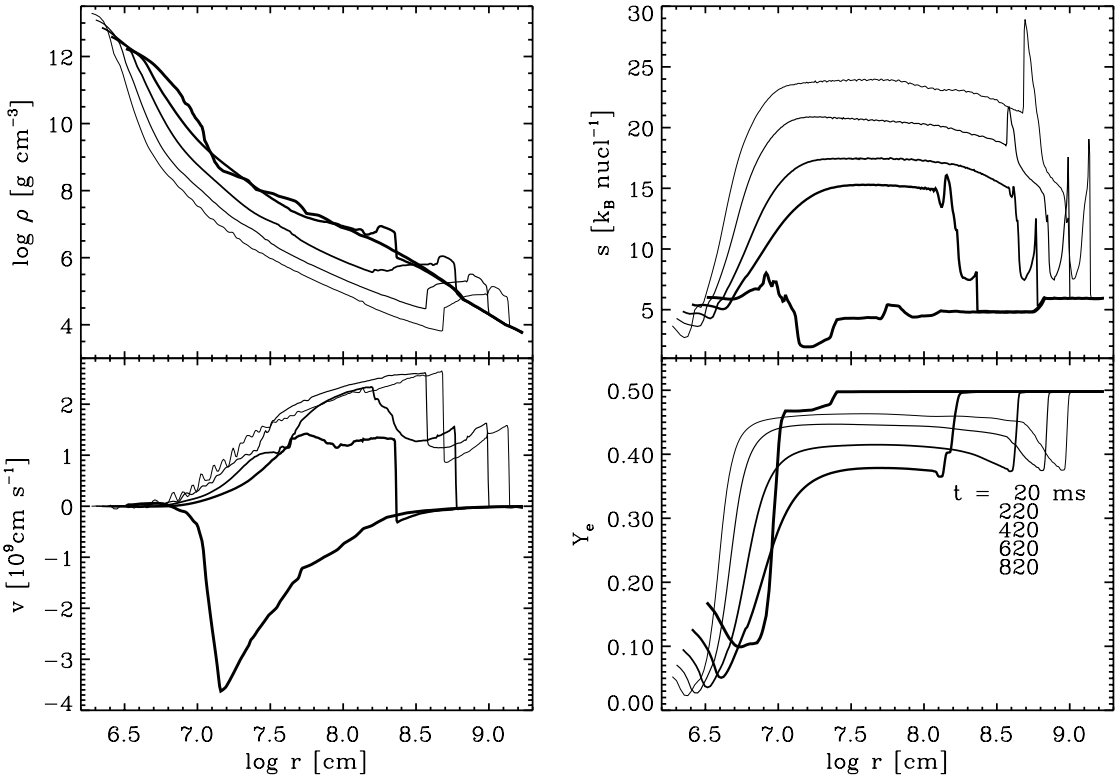

Fig. 3. Snapshots of the density, entropy, velocity and electron fraction distribution in Model O310, 20 ms (heaviest line), 220 ms, 420 ms, 620 ms and 820 ms after core bounce.

the physical conditions for their occurrence in turn, focusing first on ^{56}Ni-synthesis.

The left panels of Fig. 4 show the evolution of the density and temperature distribution for Model O310 as a function of the enclosed (baryonic) mass. The inner edge of the high-density shell is stationary at a mass coordinate of $M_r \approx 1.27\,M_\odot$. This mass shell marks the border between low and high-Y_e material in the expanding ejecta for times $t \geq 120$ ms (right lower panel of Fig. 4), i.e. for the epoch of ^{56}Ni formation. Since ^{56}Ni synthesis requires temperatures in the range of $\sim(5-7)\times10^9$ K and electron fractions $Y_e > 0.49$, we can expect that in Model O310 ^{56}Ni does not form in large amounts in regions with mass coordinates $<1.27\,M_\odot$, where $Y_e \ll 0.49$. This is confirmed by Fig. 5, which shows the composition 820 ms after bounce, when the post-shock temperature has already dropped below 2.1×10^9 K (compare Fig. 4) and nuclear reactions have frozen out. Large ^{56}Ni mass fractions (≥20%) are indeed only found for $1.27\,M_\odot \leq M_r \leq 1.37\,M_\odot$, i.e. they are confined to the dense shell. In total, $0.08\,M_\odot$ of ^{56}Ni are synthesized in Model O310. Of these, $0.04\,M_\odot$ are produced by shock-induced Si-burning in the presupernova's silicon shell (whose inner boundary was initially located at $1.32\,M_\odot$). The remaining $0.04\,M_\odot$ stem from the recombination of photodisintegrated iron core matter with high electron fraction at mass coordinates between $1.27\,M_\odot$ and $1.32\,M_\odot$. Between the neutron star surface and the inner boundary of the dense shell, i.e. for $1.14\,M_\odot \leq M_r \leq 1.27\,M_\odot$, $0.13\,M_\odot$ of material freezes out with $Y_e < 0.49$. About $0.087\,M_\odot$ of this matter end up in the neutronization tracer nucleus (denoted by X in Fig. 5). The rest, which contains also a small contribution of ^{56}Ni, is mainly made up of α-particles, ^{44}Ti, ^{48}Cr, and ^{52}Fe, i.e. the products of α-rich freezeout in high-entropy (low-density) material.

Table 4. Final total elemental yields (in $M_\odot$) for Models O310 and T310. Exponents are given in brackets.

	^{4}He	^{12}C	^{16}O	^{20}Ne	^{24}Mg
O310	5.3(+0)	1.2(–1)	1.9(–1)	4.5(–2)	5.9(–3)
T310	5.3(+0)	1.2(–1)	1.9(–1)	4.5(–2)	6.1(–3)
	^{28}Si	^{32}S	^{36}Ar	^{40}Ca	^{44}Ti
O310	8.6(–2)	2.2(–2)	6.2(–3)	6.2(–3)	4.6(–3)
T310	8.5(–2)	2.3(–2)	6.6(–3)	6.5(–3)	5.0(–3)
	^{48}Cr	^{52}Fe	^{56}Ni	X	
O310	3.6(–3)	3.7(–3)	8.0(–2)	8.7(–2)	
T310	3.9(–3)	4.0(–3)	7.5(–2)	1.0(–1)	

Table 4 gives an overview of the nuclear yields for our explosion models (not including effects of eventual fallback). For a discussion of their accuracy regarding numerical diffusion, see Kifonidis et al. (2001), and Plewa & Müller (1999) who analyzed the effect in detail, especially for the case of ^{44}Ti. With the spatial resolution used in the explosion models presented in this paper, the bulk of ^{44}Ti is synthesized between about 400 ms and 700 ms after core bounce at $1.29 \leq M_r \leq 1.36\,M_\odot$, in a layer where the abundance of α-particles decreases and ^{40}Ca comes up (Fig. 5). However, if the spatial resolution is increased, and thus numerical diffusion at the ^{4}He/^{40}Ca boundary is reduced, the width of the layer of ^{44}Ti production via the reaction ^{40}Ca$(\alpha,\gamma)^{44}$Ti is narrowed. This decreases the ^{44}Ti yield by up to a factor of 3 (Kifonidis et al. 2001).

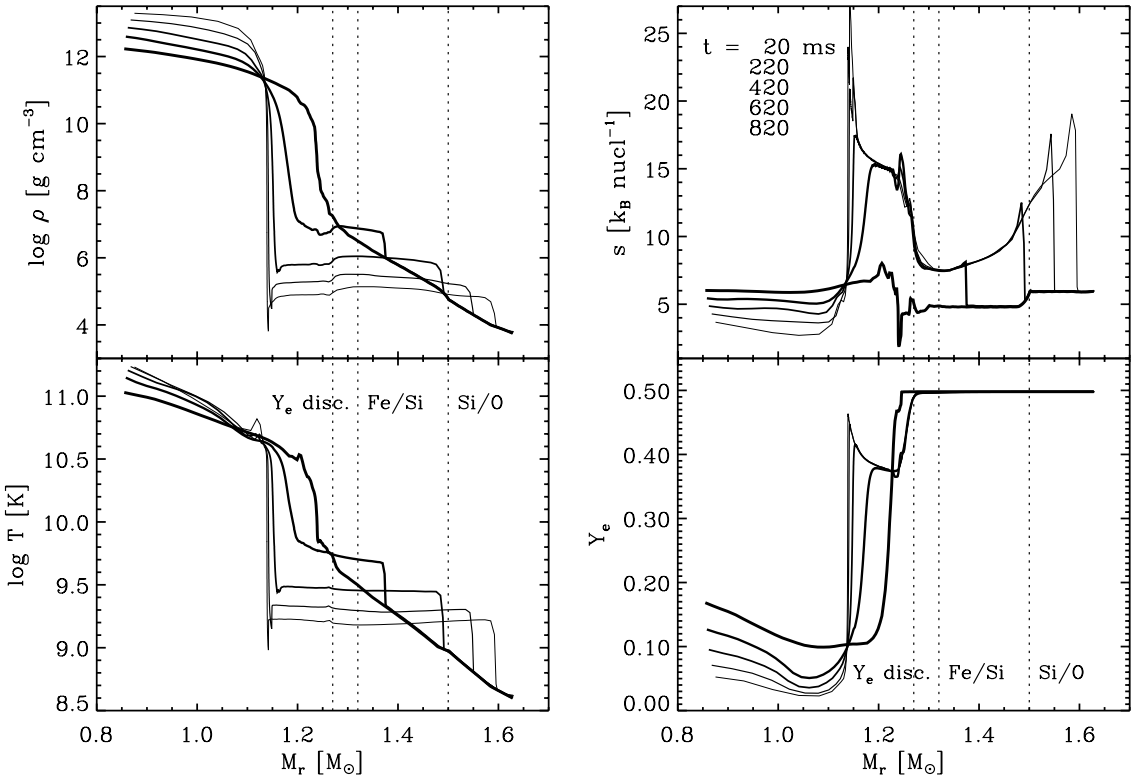

Fig. 4. Evolution of density, temperature, entropy and electron fraction as functions of the enclosed mass for Model O310 between $t = 20$ ms and $t = 820$ ms post-bounce. The positions of the Fe/Si and Si/O interfaces, and the Y_e discontinuity (see text) are indicated by dotted vertical lines.

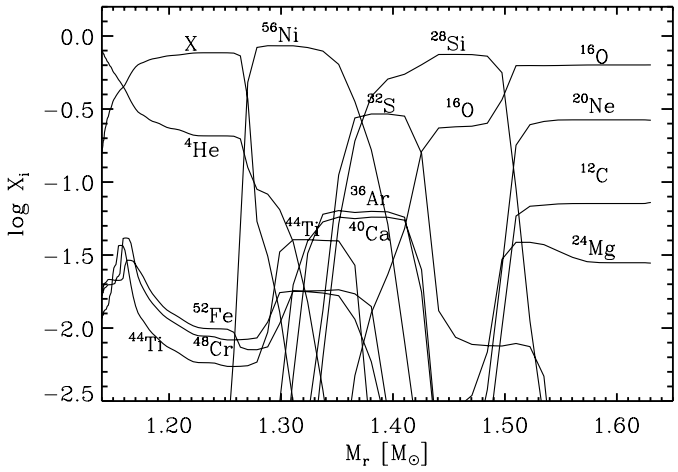

Fig. 5. Chemical composition of Model O310 versus mass at $t = 820$ ms. X denotes the neutronization tracer nucleus.

The yield of ^{56}Ni is much less sensitive to numerical diffusion. However, it cannot be determined to much higher accuracy than that of ^{44}Ti because the contribution of the region with $Y_e < 0.49$ to the ^{56}Ni production depends sensitively on the ratio of the ν_e and $\bar{\nu}_e$ luminosities, $L_{\nu_e}/L_{\bar{\nu}_e}$, and its evolution with time. This ratio, which determines the electron fraction in regions close to the gain radius through neutrino-matter interactions (Janka & Müller 1996, and references therein), must be regarded as uncertain in calculations like ours, that do not use accurate neutrino transport. With the parameters adopted for Model O310 we observe that $Y_e \ll 0.5$ for $M_r < 1.27\,M_\odot$. However, given a higher $L_{\nu_e}/L_{\bar{\nu}_e}$ the opposite may occur, with Y_e being increased in the neutrino-heated layers to values up to and even above 0.5, as seen in recent calculations including Boltzmann neutrino transport (Janka et al. 2003). If this were the case, the composition would be dominated by ^{56}Ni also for $1.16\,M_\odot \le M_r \le 1.27\,M_\odot$, while only insignificant amounts of neutron-rich nuclei would be synthesized in these layers. Hence, the ^{56}Ni yield might be increased by a factor of up to about 2 compared to Model O310.

Just interior to the dense shell (and the ^{56}Ni-rich zone in Model O310), we must expect substantial convective activity to occur, because neutrino-matter interactions sustain a negative entropy gradient in the neutrino-heated material throughout the entire evolution up to 820 ms. As Fig. 4 shows, the entropy starts to rise steeply when one moves inward from $1.27\,M_\odot$ and reaches a maximum near the gain radius (and at times later than 0.5 s at a position just downstream of the reverse shock). This negative entropy gradient will give rise to convective motions that, in contrast to the one-dimensional situation, will mix high-entropy, low-Y_e, matter from the deeper layers of the iron-core with lower-entropy, high-Y_e, material of the outermost iron core and the silicon shell. We discuss the implications of this in more detail in the next section.

Finally, we wish to draw attention to the outer boundary of the dense shell. Figures 4 and 6 indicate that after about 500 ms this boundary coincides with the star's Si/O interface. A pronounced negative density gradient forms at this interface which is accompanied by a positive pressure gradient (Fig. 6). Such a configuration is Rayleigh-Taylor unstable even in the absence

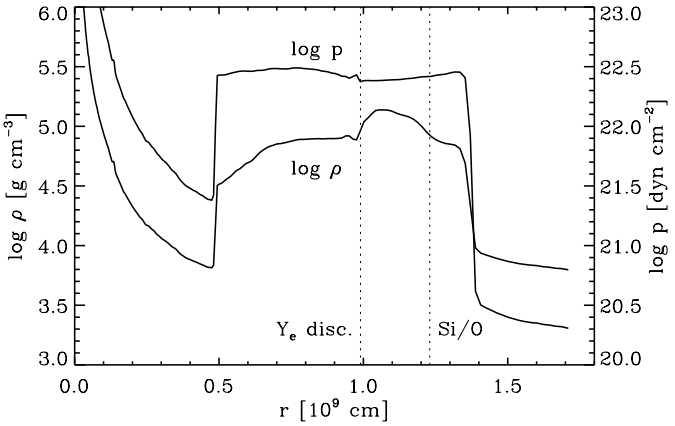

Fig. 6. Density and pressure profiles of Model O310 at $t = 820$ ms. The position of the Y_e discontinuity and of the Si/O interface are indicated by dotted vertical lines. Note the dense shell at $r = 1.1 \times 10^9$ cm, and the density and pressure gradients of opposite signs for 1.05×10^9 cm $\leq r \leq 1.35 \times 10^9$ cm.

of gravity (Chevalier 1976). Its rather close spatial proximity to the convectively unstable layers at the inner edge of the dense shell is of decisive importance for the further evolution of the models.

5.2. Evolution in two dimensions

Repeating the calculation of the one-dimensional model O310 in two dimensions we obtained Model T310 that develops convective activity already 60 ms after core bounce. Fingers of buoyant, high-entropy material with $Y_e \approx 0.4$, and an initial angular width of about $5^\circ - 10^\circ$ form quickly from the imposed seed perturbations in the neutrino heated layer near the gain radius and start to rise toward the shock into the surrounding gas of lower entropy. While doing so they acquire a mushroom-capped shape and display a tendency to merge into bubbles of about $10^\circ - 20^\circ$ lateral width (Fig. 1). Between the bubbles, low-entropy material with $Y_e \approx 0.498$ sinks inward in tube-like flows. Compared to the one dimensional case, the convective rise of the high-entropy gas leads to a somewhat more efficient energy transport, and a reduced energy loss by the reemission of neutrinos from heated matter. Therefore Model T310 exploded with an energy of $E_{\rm exp} = 1.77 \times 10^{51}$ erg, which is 11% higher than in Model O310. The mean shock expansion velocity is, however, almost the same as in Model O310.

While the shock propagates through the Si-rich layers of the star, ^{56}Ni is synthesized in the high-density shell (Sect. 5.1), which is distorted at its base by the rising bubbles of high-entropy material. As in the one-dimensional case, freezeout of nuclear reactions in the deleptonized bubbles leads to high abundances of the neutronization tracer and to smaller yields for nuclei produced by α-rich freezeout. However, in between the bubbles, i.e. in the down-flows mentioned above, electron fractions are sufficiently high that ^{56}Ni is synthesized. Hence, the inner boundary of the ^{56}Ni shell possesses an aspherical shape closely tracing the inner edge of the low-entropy (high-density) material in the convective region, while the outer ^{56}Ni-boundary coincides with the (spherical) shock wave as long as the post-shock temperatures stay above 5×10^9 K. After complete silicon burning has ceased at $t \approx 270$ ms, an anisotropic nickel shell is left behind, while the spherical shock continues moving outward (see Fig. 1).

The differences in the spatial nickel distribution between Model T310 and its 1D analogue, Model O310, are relatively small, however. This is caused by the high initial neutrino luminosities and their rapid, exponential decline (Eq. (1)) adopted for our models. Both assumptions favour small explosion time scales which prevents convective bubbles to merge to large-scale structures, as in cases where the phase of convective overturn lasts for several turn-over times. Lowering the neutrino luminosities (and the explosion energies), we obtain stronger convection that largely distorts the shock wave by developing big bubbles of neutrino-heated material (see Janka & Müller 1996; Kifonidis et al. 2000, 2001; and Janka et al. 2001 for examples). Adopting constant core luminosities in contrast to the exponential law of Eq. (1), we can produce models that exhibit the vigorous boiling behaviour reported by Burrows et al. (1995). Such cases can finally develop global anisotropies, showing a dominance of the $m = 0$, $l = 1$ mode of convection (see Janka et al. 2003; Scheck et al., in preparation). As a consequence, convection can lead to huge deviations of the spatial distribution of iron group nuclei from spherical symmetry, much stronger than those visible in Fig. 1. Convection can also change the nucleosynthetic yields of iron group nuclei, because it enhances neutronization by cycling high-Y_e material from outer layers through the regions near the gain radius where the gas loses lepton number (Kifonidis et al. 2001; Janka et al. 2001). Due to our adopted ν_e and $\bar{\nu}_e$ luminosities the gas cannot regain high Y_e values when it moves outward again. This leads to ^{56}Ni yields that are about 6% smaller in Model T310 as compared to the 1D case, Model O310, while the final yield of the neutronization tracer shows the opposite behaviour and is 15% larger in Model T310 than in Model O310. These effects are comparatively small in Model T310, again mainly due to the short explosion time scale of this model.

The distribution of the elements in velocity space is of significant importance for an understanding of the evolution of the supernova beyond the first second. Since Models O310 and T310 barely differ in this respect we discuss only the two-dimensional case. In Fig. 7 we plot as functions of the radial velocity v_r and time, the fractions of the total mass of ^{16}O, ^{28}Si, ^{44}Ti and ^{56}Ni that are contained within the velocity intervals $[v_r, v_r + {\rm d}v_r]$ with ${\rm d}v_r = 350\,{\rm km\,s^{-1}}$. At $t = 120$ ms, when the shock is travelling through the outermost layers of the iron core, substantial amounts of material from the silicon and oxygen shells are either still near hydrostatic equilibrium or falling towards the shock. Consequently the peak and wings of the mass distributions of the respective elements have zero and negative velocities. As the post-shock temperature begins to drop below 7×10^9 K, reassembly of α-particles to heavier nuclei starts in the immediate post-shock region and leads to initially small abundances of ^{44}Ti and ^{56}Ni, the bulk of which has velocities around $8 \times 10^3\,{\rm km\,s^{-1}}$.

Only 100 ms later ($t = 220$ ms) the explosion gains momentum, and the shock propagates through the silicon shell and encounters substantially smaller maximum infall velocities of

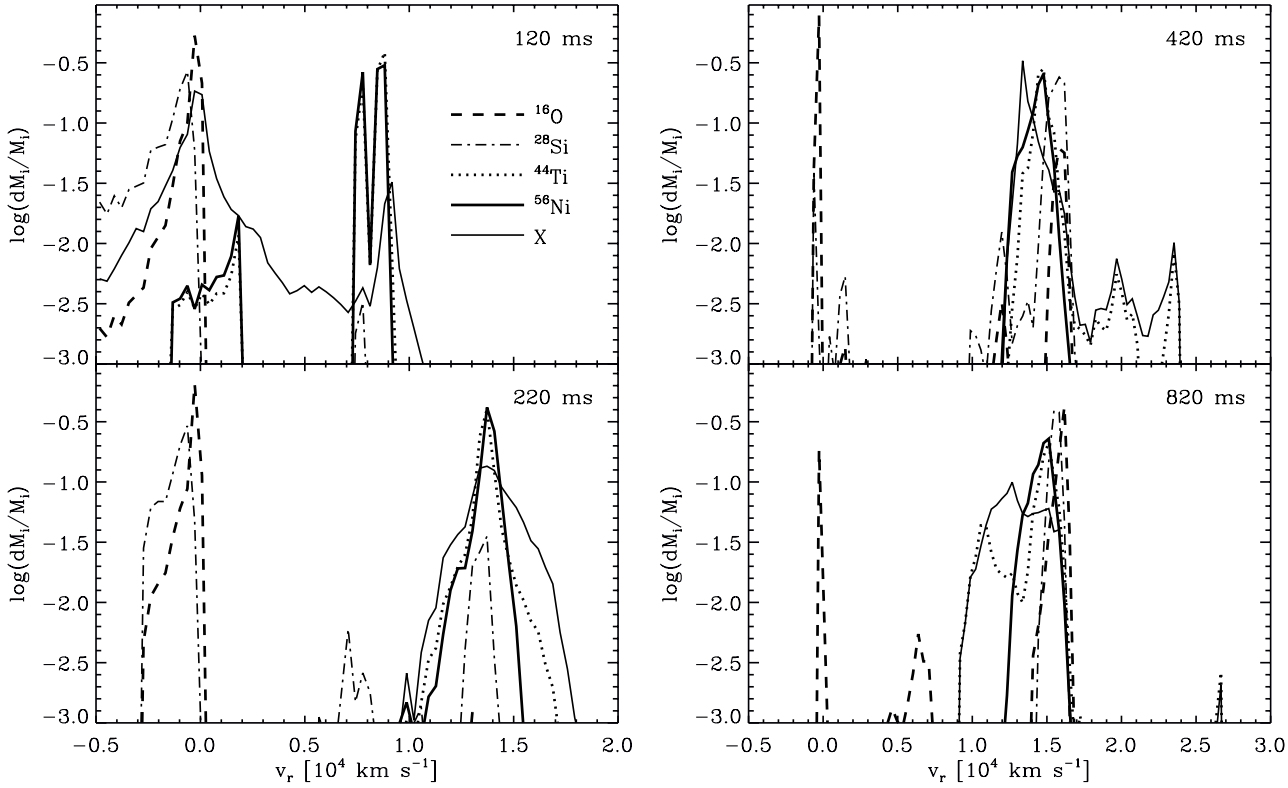

Fig. 7. Fractional mass of different elements contained within the velocity interval $[v_r, v_r + dv_r]$ as a function of the radial velocity v_r in Model T310. The resolution is $dv_r = 350\,\mathrm{km\,s^{-1}}$.

only $3000\,\mathrm{km\,s^{-1}}$. This leads to the cutoff of the high velocity wings of silicon and oxygen at $-3 \times 10^3\,\mathrm{km\,s^{-1}}$. Downstream of the shock, ^{56}Ni is synthesized as the dominant nucleus in regions of explosive silicon burning, while also ^{44}Ti is built up in smaller amounts. The spatial neighborhood of these two nuclei is reflected in their velocity distributions, which both peak around $1.35 \times 10^4\,\mathrm{km\,s^{-1}}$. However, in contrast to ^{56}Ni, some ^{44}Ti also forms by α-rich freezeout in the rising convective blobs that at this stage show the highest velocities on the grid. This causes the broad wing in the velocity distribution of ^{44}Ti up to $1.7 \times 10^4\,\mathrm{km\,s^{-1}}$, while maximum ^{56}Ni velocities reach $1.55 \times 10^4\,\mathrm{km\,s^{-1}}$. The velocity distribution for the neutronization tracer shows a behaviour similar to ^{44}Ti.

At 420 ms the supernova's explosion energy is still increasing and has led to maximum ^{56}Ni velocities as high as $1.65{\times}10^4\,\mathrm{km\,s^{-1}}$. Substantial amounts of silicon have also been accelerated outward. A stratification of these elements in velocity space is beginning to emerge because the positive velocity gradient behind the shock (see Fig. 3) results in higher velocities in the post-shock region as compared to gas in the deeper layers of the ejecta. Meanwhile, the neutrino-driven wind has begun to blow off material from the proto-neutron star surface with velocities in excess of $2.0 \times 10^4\,\mathrm{km\,s^{-1}}$ (Fig. 3). Traces of ^{44}Ti in the wind, that has a composition dominated by α-particles and neutron-rich nuclei, can be seen at these velocities. The distribution of ^{44}Ti in velocity space is somewhat uncertain. We have noted in Sect. 5.1 that the bulk of ^{44}Ti is synthesized at the boundary of layers with high ^{4}He and ^{40}Ca abundances. The location of this region coincides with the maximum of the ^{56}Ni abundance (Fig. 5). Thus, the peaks of both elements are found at comparable velocities ($\sim 1.4{\times}10^4\,\mathrm{km\,s^{-1}}$; Fig. 7). We note again, however, that the spatial distribution and the yield of ^{44}Ti are severely affected by numerical diffusion (Plewa & Müller 1999). The location of the ^{44}Ti peak at $t = 420$ ms (Fig. 7) might actually occur at much lower velocities, if numerical diffusion (and thereby ^{44}Ti synthesis at the ^{4}He/^{40}Ca boundary) is substantially reduced. In this case, the contribution from the slower, deeper layers of the ejecta, just downstream of the reverse shock, might dominate. Indeed this material causes the second, smaller ^{44}Ti peak near $1.0 \times 10^4\,\mathrm{km\,s^{-1}}$ at $t = 820$ ms (lower right panel of Fig. 7).

The velocities of the fastest regions that contain ^{56}Ni reach a maximum of $1.7 \times 10^4\,\mathrm{km\,s^{-1}}$ around $t = 620$ ms and decrease slightly to $1.65 \times 10^4\,\mathrm{km\,s^{-1}}$ at $t = 820$ ms. It is obvious, that these ^{56}Ni velocities are much larger than those observed in SN 1987 A and that some slow-down of this material must have taken place later. In fact, we will show in Sect. 6.2 that excessive deceleration of this material during the subsequent evolution is the main problem for an explanation of the observed ^{56}Ni velocities in SN 1987 A.

Summarizing our one and two-dimensional results for the evolution within the first second, we note that a Rayleigh-Taylor unstable density inversion can form at the Si/O interface of a blue supergiant. The quickly expanding ^{56}Ni is situated just interior to this interface and is distributed anisotropically in an inhomogeneous layer. This results in a seed perturbation for the

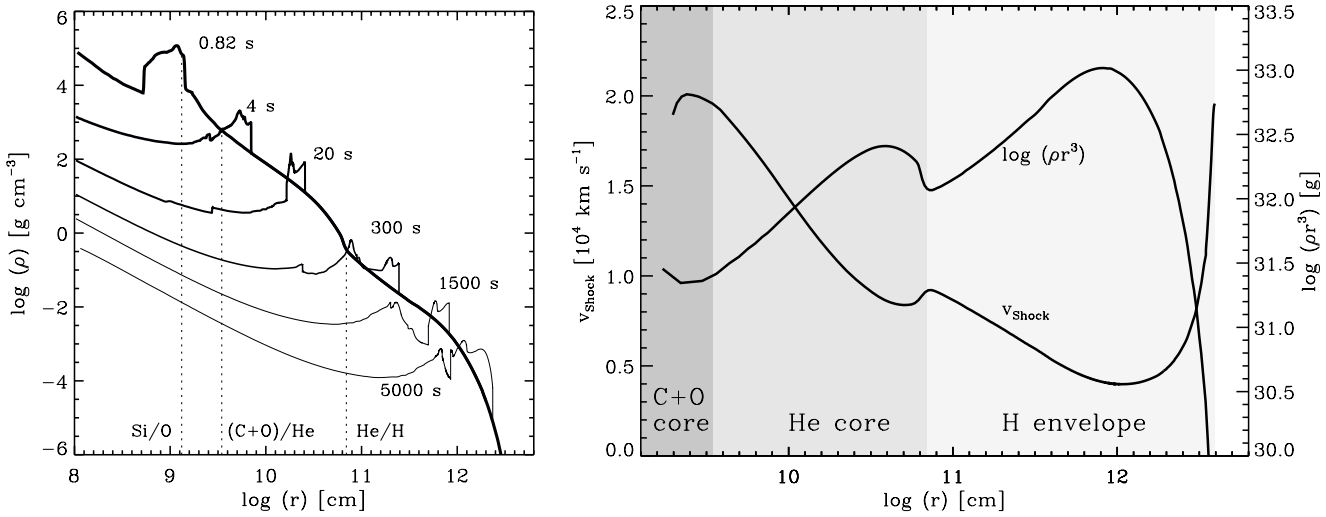

Fig. 8. a) Evolution of the density in our one-dimensional type II supernova simulation Model $\overline{\text{T310}}$ (left). The dotted lines indicate the positions of the Si/O, (C+O)/He and He/H interfaces 0.82 s after core bounce. **b)** Shock velocity as a function of shock radius in Model $\overline{\text{T310}}$, and radial dependence of ρr^3 for our progenitor model (right). Note the deceleration of the shock after it has crossed the (C+O)/He interface at $\log(r/\text{cm}) = 9.55$ and the He/H interface at $\log(r/\text{cm}) = 10.85$. The increase of the shock velocity for $\log(r/\text{cm}) \geq 12.2$ is due to the steep drop of the density in the atmosphere of the star.

Rayleigh-Taylor unstable regions. We will show in the following sections that the magnitude of this perturbation is sufficient to induce significant outward mixing of ^{56}Ni.

6. Beyond the first second: A type II model

6.1. One-dimensional evolution

Once the shock wave has been launched by neutrino heating and the explosion energy has saturated, the further evolution of the supernova depends strongly on the density profile of the progenitor star. According to the analytic blast wave solutions of Sedov (1959), the shock decelerates whenever it encounters a density profile that falls off with a flatter slope than $\propto r^{-3}$ (i.e. for increasing ρr^3), while for density profiles steeper than $\propto r^{-3}$ (i.e. for decreasing ρr^3) it accelerates. Since models of supernova progenitors (see e.g. Woosley & Weaver 1995) do not show a density structure that can be described by a single power-law, an unsteady shock propagation results that in turn gives rise to Rayleigh-Taylor unstable pressure and density gradients at the composition interfaces of the star. In this section we follow shock propagation beyond the first second with our AMR code in one spatial dimension to illustrate these effects. In order to obtain the closest possible approximation to the energetics of the two-dimensional case, with which we will compare our results in the following section, we start this 1D calculation from an angularly averaged version of our 2D explosion, Model T310, (instead of the one-dimensional model O310). We will henceforth refer to the one-dimensional results of this section as Model $\overline{\text{T310}}$.

Figure 8a displays the evolution of the density for this model. The locations of the Si/O, (C+O)/He, and He/H interfaces at the start of the calculation (i.e. 0.82 s after bounce) are also indicated. In Fig. 8b we show the shock velocity as a function of shock radius for times later than about one second after core bounce, along with the radial variation of ρr^3 for our progenitor model. When the shock wave crosses the (C+O)/He interface at $\log(r/\text{cm}) = 9.55$, 1.8 s after bounce, its propagation speed is as high as $\sim$20 000 km s^{-1}. Thereafter, a rapid decrease of the shock velocity can be seen, since ρr^3 increases, i.e. the density profile in the He core falls off with a more shallow slope than $\propto r^{-3}$. The deceleration lasts until the blast wave has reached the outer layers of the He core and enters a narrow region of decreasing ρr^3 around $\log(r/\text{cm}) = 10.7$. This region is characterized by a rapid drop of the density just below the He/H interface (see Fig. 8a). Here the shock temporarily accelerates to about 9000 km s^{-1} (Fig. 8b). Once it has passed the He/H interface around 80 s after core bounce, the evolution resembles that after the crossing of the (C+O)/He interface. A gradual deceleration of the shock to 4000 km s^{-1} occurs, until the blast wave enters the atmosphere of the star and finally accelerates to more than 20 000 km s^{-1}, while propagating off the numerical grid.

Every time the shock decelerates, it leaves behind a positive pressure gradient which slows down the post-shock layers. The shocked material thus piles up and forms a high-density post-shock shell. Note that layers which are sufficiently far downstream of the shock may be out of sonic contact with it, i.e. on the time scale of the supernova expansion these layers may not be reached by sound waves originating in the immediate post-shock region. In this case, the only way in which information can be mediated to the deeper layers is through a supersonic wave. Therefore their slow-down proceeds via a reverse shock, that forms at the inner boundary of the high-density shell of decelerated matter and starts to propagate inwards in mass. The reverse shocks as well as the dense shells that form after the main shock has passed the Si/O, (C+O)/He and He/H interfaces, can be clearly seen in Fig. 8a in the density structures for 0.82 s, 20 s and 1500 s, respectively. It is also apparent that the density profiles for the latter two times show a striking similarity in the region that is bounded by the forward and the reverse shocks.

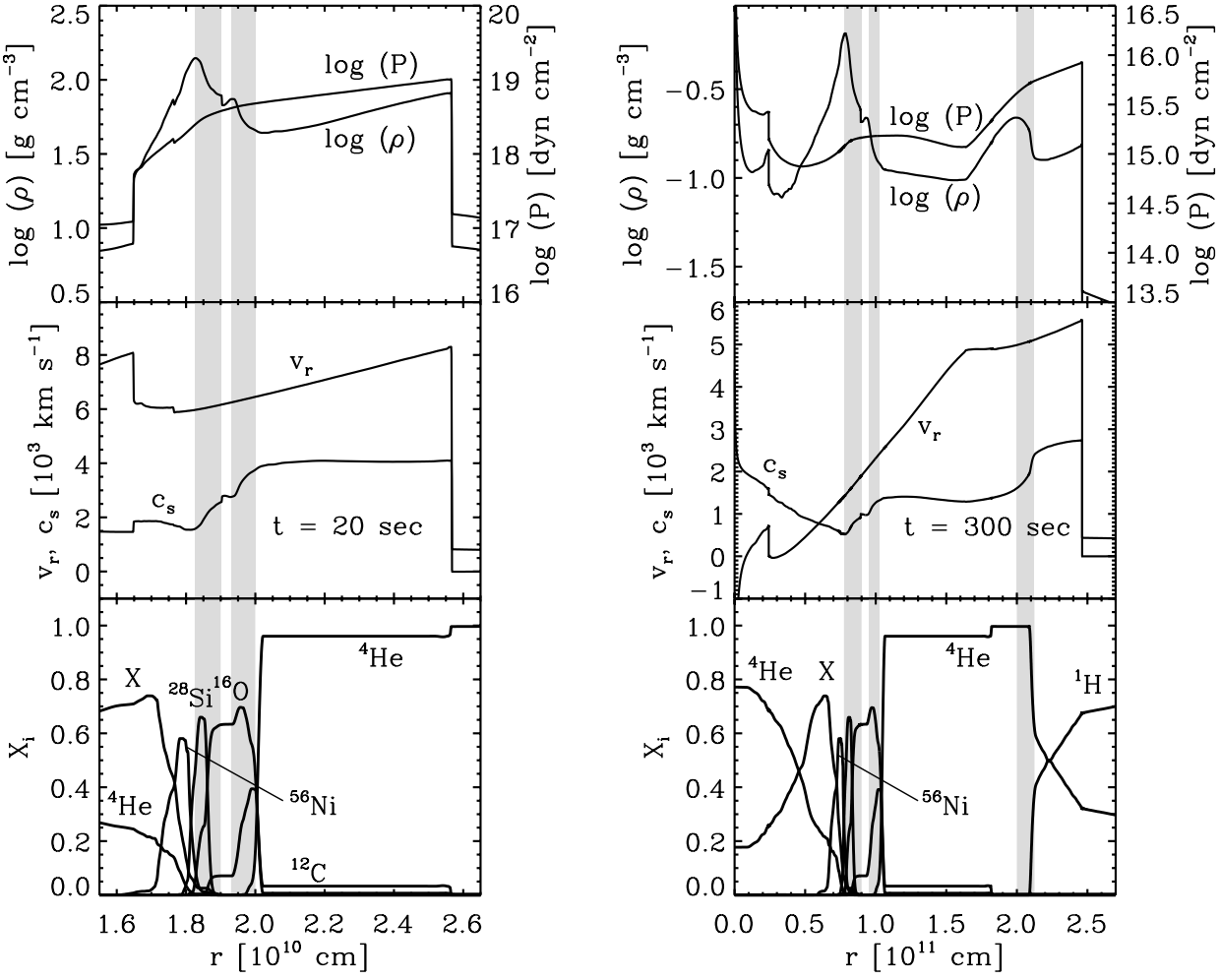

Fig. 9. Structure of Model $\overline{\text{T310}}$, **a)** 20 s (left), and **b)** 300 s after bounce (right). Shown are (from top) the density, pressure, velocity, sound speed, and mass fractions as functions of radius. Note the unstable regions (shaded in grey) near the Si/O, (C+O)/He and He/H composition interfaces, where the density and pressure gradients have opposite signs. At $t = 300$ s, the density gradient at the inner edge of the dense shell that has formed below the He/H interface is in the process of steepening into a reverse shock (compare also Fig. 8a). Note also the enormous drop of the velocity in the layers that are enriched in ^{56}Ni, from 6000 km s^{-1} at 20 s to 1300 km s^{-1} at 300 s.

In a one-dimensional calculation, where hydrodynamic instabilities are absent, dense shells, that have formed during earlier phases of the evolution, are preserved provided the numerical diffusivity of the employed hydrodynamic scheme is sufficiently small. This is demonstrated by the left panel of Fig. 9 which shows some flow quantities 20 s after core bounce. Note that two high-density peaks are visible between the forward and reverse shock at that time. The inner is the one that formed at the Si/O interface (Sect. 5.1). It contains mainly silicon and oxygen. The outer one has formed at the (C+O)/He interface and contains carbon and oxygen. In the layers of these shells that are shaded in gray in Fig. 9, negative density and positive pressure gradients exist. Thus, already at this early time, Rayleigh-Taylor instabilities may grow in these regions (Chevalier 1976). This is confirmed quantitatively by performing a linear stability analysis (see e.g. Müller et al. 1991b; Iwamoto et al. 1997, and the references therein; note that our calculations differ from these previous simulations because we start from a model that has a consistent explosion history, instead of having the explosion energy artificially deposited in the stellar core).

In Fig. 10 we plot for different times the total, time-integrated growth rate

$$\frac{\zeta}{\zeta_0} = \exp\left(\int_0^t \sigma \mathrm{d}t'\right), \tag{2}$$

i.e. the factor by which a (small) perturbation with an initial amplitude ζ_0 would be magnified at time t according to linear perturbations theory. The growth rate of the instability, σ, is given by

$$\sigma = \sqrt{-\frac{P}{\rho}\frac{\partial \ln P}{\partial r}\frac{\partial \ln \rho}{\partial r}}, \tag{3}$$

(e.g. Müller et al. 1991b), where we have assumed the fluid to be incompressible for simplicity. Within only 20 s after bounce, the amplification factor grows to about 10^6 in both unstable regions, which are separated by a narrow stable layer at 1.6 $M_\odot$. Both growth rates are increasing until 300 s after bounce and

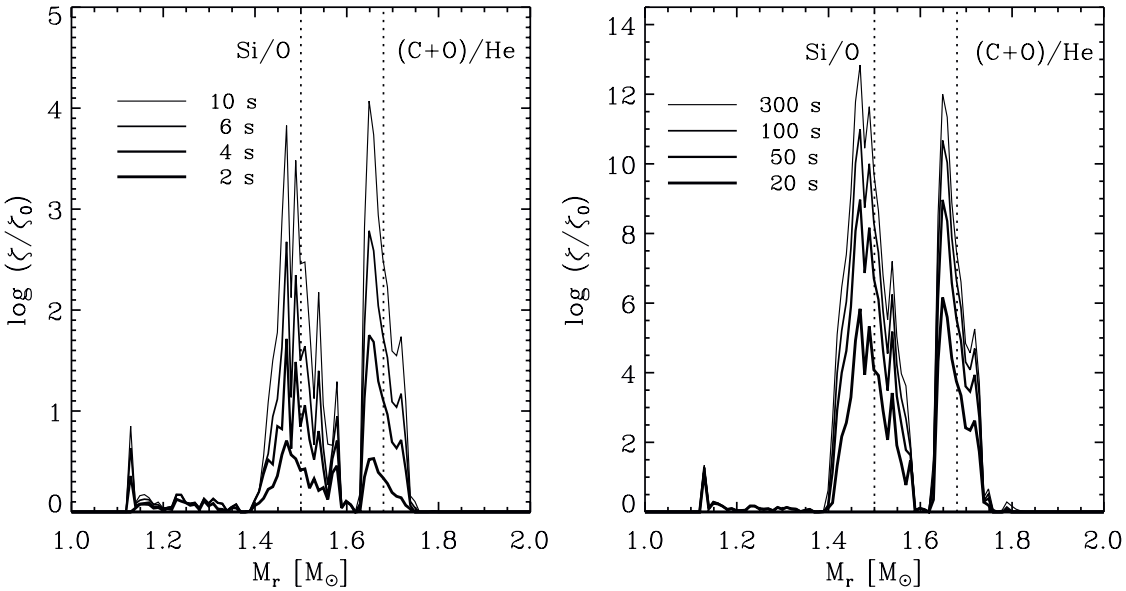

Fig. 10. Logarithm of the total, time-integrated, *linear* growth rate in the unstable layers near the Si/O and (C+O)/He composition interfaces of Model T310 at different times. The linear growth rates increase with time and reach amplification factors $\geq 10^{12}$ within the first 300 s (i.e. five minutes) of the explosion.

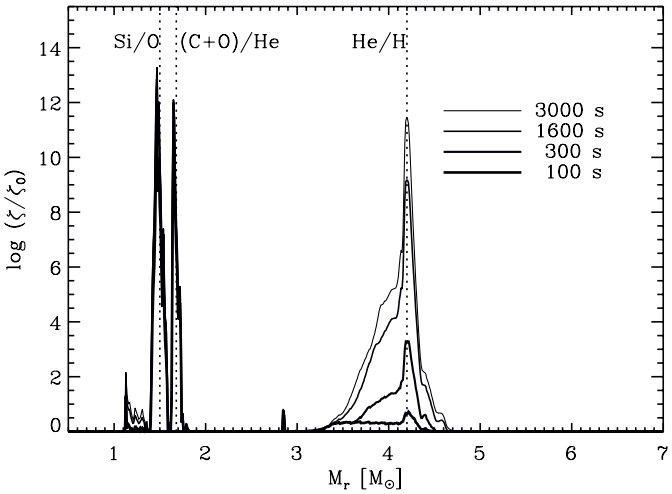

Fig. 11. Logarithm of the total, time-integrated, *linear* growth rate in the unstable layers near the Si/O, (C+O)/He and He/H composition interfaces of Model T310 at different times. Comparing the amplitudes of the growth rates at the Si/O and (C+O)/He interfaces with those given in Fig. 10 one can see that these have saturated after 300 s (in fact the curves for 300 s, 1600 s, and 3000 s are not visible individually because they are identical within plotting accuracy). Note, however, that the rate for the instability at the He/H interface is still increasing between 300 s and 3000 s.

saturate thereafter. The right panel of Fig. 9 shows that at $t = 300$ s the metal core of the star has piled up to a high-density zone that includes the two unstable interfaces. At this time, the shock has already passed the He/H interface and a third unstable region has formed at the outer edge of the dense shell that the shock has left behind at the He/H interface. The evolution of the growth rate in this region is shown in Fig. 11. At $t = 300$ s it is much smaller than the rates for the instabilities at the Si/O and (C+O)/He interfaces. However, while the latter reach their maxima at this epoch, the growth rate at the He/H interface still increases. It reaches about the same level as the growth rates at the two inner interfaces at 3000 s after core bounce.

This behaviour is opposite to that found in the calculations of Müller et al. (1991b), where the instability initially grows faster at the He/H interface and only after some time is surpassed by the growth at the (C+O)/He interface. It is very likely, that this result of Müller et al. (1991b) is caused by the fact that they started their stability analysis as well as their 2D calculations 300 s after core bounce. *Reliable calculations of the Rayleigh-Taylor growth, however, require consideration of the very early moments of the explosion*. While the results of the linear stability analysis are certainly invalid quantitatively once non-linear growth sets in, the above conclusion is substantiated by our two-dimensional calculations. It is also supported by results of Iwamoto et al. (1997) who found a similar behaviour for the growth of the instability at the (C+O)/He and He/H interfaces of their 2D models for SN 1993 J.

To our knowledge, large growth rates for Rayleigh-Taylor instabilities at the Si/O interface of a massive star have never been reported before. We can only speculate about the reason for the absence of this unstable layer in previous simulations. Either it was caused by the fact that the explosion was initiated artificially by depositing energy in an ad hoc way, or it was caused by insufficient numerical resolution, or by differences in the structure of the progenitor stars that were employed in these studies. The latter is obviously the case for the simulations of Arnett et al. (1989b), Fryxell et al. (1991) and Müller et al. (1991b) who used a stellar model at the end of carbon burning for their calculations. Also a combination of the effects listed above is possible. High-resolution studies with our hydrodynamic code applied to different progenitor models may be required to clarify this issue. We stress this point because

the two-dimensional models to be discussed in the next section demonstrated that the instability at the Si/O interface *is the most crucial one* for determining the subsequent evolution.

6.2. Two-dimensional evolution

6.2.1. Clump formation and mixing

In contrast to the one-dimensional case, in two (and three) spatial dimensions the dense shells that form at the composition interfaces can fragment into a set of smaller clumps that may decouple from the flow and move ballistically through the ejecta. Such a fragmentation actually occurs in our models due to the spatial proximity of the Rayleigh-Taylor unstable zones near the Si/O and (C+O)/He interfaces and the convective layers. To demonstrate these effects, we present a two-dimensional type II supernova calculation that was started from the shock-revival model T310. In what follows we will refer to this simulation as Model T310a. To illustrate its hydrodynamic evolution we show plots[1] of the mass density and the partial densities of the nuclei ^{16}O, ^{28}Si and ^{56}Ni.

Figure 12a displays the situation 4 s after core bounce, when the supernova shock has already crossed the (C+O)/He interface of the star. The anisotropic structures that can be seen in this figure are strikingly similar to those visible 420 ms after bounce (Fig. 1b). This indicates that the low-density (high-entropy) layers of the ejecta, that were heated by neutrinos, expand essentially self-similarly during the first few seconds of the explosion. However, outside of the high-entropy mushrooms, and exactly as in the one-dimensional case, material of the Si and C+O layers of the star piles up in two dense shells. Ten seconds after core bounce (Fig. 12b) also the high-entropy gas is affected, and the low-density mushrooms have been compressed to flat structures. Only 10 s later (Fig. 12c) the compression has become so strong that the density distribution no longer resembles the flow-structures of the shock revival phase. A second reverse shock has formed as a consequence of the deceleration of the main shock in the He core (Sect. 6.1). It is visible as the dark discontinuity at $r = 1.6 \times 10^{10}$ cm in Fig. 12c. The initial mushrooms have imprinted a strong long-wavelength perturbation both on the dense shell behind the Si/O interface and at the (C+O)/He interface. Superposed upon this perturbation, small-scale disturbances start to grow along the entire Si/O interface where also about 10 cusps (not counting the features near the symmetry axis) begin to develop that are located about 20° apart. Interestingly, the positions of these cusps do *not* coincide with those of the former mushrooms that are located in the regions *between* the cusps. The cusps themselves seem to be pushed by the denser material that constituted the former down-flows between the mushrooms. It is exactly in these dense regions, where ^{56}Ni had formed during the first 250 ms of the explosion. Although most of the ^{56}Ni is originally located in a layer just interior to the unstable zone at the Si/O interface (see Fig. 12a and compare also Fig. 9 for the one-dimensional model), the dense regions with their larger momentum cannot be slowed down as strongly as their neighbouring matter so that they penetrate outward much farther. This becomes evident in the plots for $t = 100$ s (Fig. 13a). The cusps have already grown into separate fingers that start to rise through the (C+O)/He interface and impose a long-wavelength perturbation onto these layers. Concurrently, the smallest scale perturbations that are resolved on our grid have grown to small mushrooms at the Si/O interface and start to mix ^{28}Si outwards while ^{16}O is mixed inwards in between them. The growth of Rayleigh-Taylor fingers from the former dense Ni-"pockets" has important consequences for the interpretation of observational data and will be addressed in more detail in Sect. 7.

At $t = 100$ s the supernova shock has already passed the He/H interface. Furthermore, the reverse shock that had formed due to the slow-down of the main shock in the He core starts to propagate inward in radius. This reverse shock decelerates the innermost layers of the ejecta until it is reflected at the inner boundary and moves outward again, compressing the inner metal core of the star (Figs. 13b and c). Five minutes after bounce, the metal core itself is totally shredded by the instability. Showing a density contrast to the ambient material of up to a factor of 5, the fingers have grown into the typical mushroom shape, which is caused by Kelvin-Helmholtz instabilities (Fig. 13b). Almost the entire metal core has thereby been carried through a substantial fraction of the He core, while in turn helium-rich gas was mixed into the metal core in "pockets" between the fingers. These low-density helium tongues can be discerned as the black regions around the blueish oxygen plumes in the abundance plots of Fig. 13. Note that there is a second helium-rich region closer to the center of the models, interior to the red, green, and blue-colored zones. This region contains material that experienced a high-entropy freeze-out of nuclear reactions, and thus shows high abundances of α-particles and nuclei like ^{44}Ti. In between this α-rich layer and the regions of ^{56}Ni dominance (the patches of dense material colored in red and pink in the abundance panel of Fig. 13; see also Fig. 9 for the one-dimensional case) one encounters neutron-rich nuclei. These nuclear species participate in the mixing. The closer they are located to the unstable interfaces, the stronger their spatial distribution is affected.

At 1500 s after bounce, the flow in the mixing region has become very complex because of the interaction of the instabilities at the former Si/O and (C+O)/He interfaces and the action of Kelvin-Helmholtz instabilities in the shear flows along the fingers (Fig. 13c). During this phase, and depending on the spatial resolution, our simulations show a tendency for the edges of the fingers to fragment into smaller structures. This fragmentation appears to be more pronounced for models with small explosion energies. In this case, the time-scale for the fingers to cross the He core may increase sufficiently to allow for substantial growth of fluid-dynamic instabilities at the boundaries of the fingers.

While the central regions of the star are turned inside out, a dense shell can be seen 1500 s after bounce just below the border between helium core and hydrogen envelope (Fig. 13c). It is this prominent shell that we also found in the one-dimensional calculation (Sect. 6.1) as a result of the deceleration of the main shock in the hydrogen envelope. Note that like in the

[1] Movies from this simulation are available under
`http://www.mpa-garching.mpg.de/~kok/MPG`

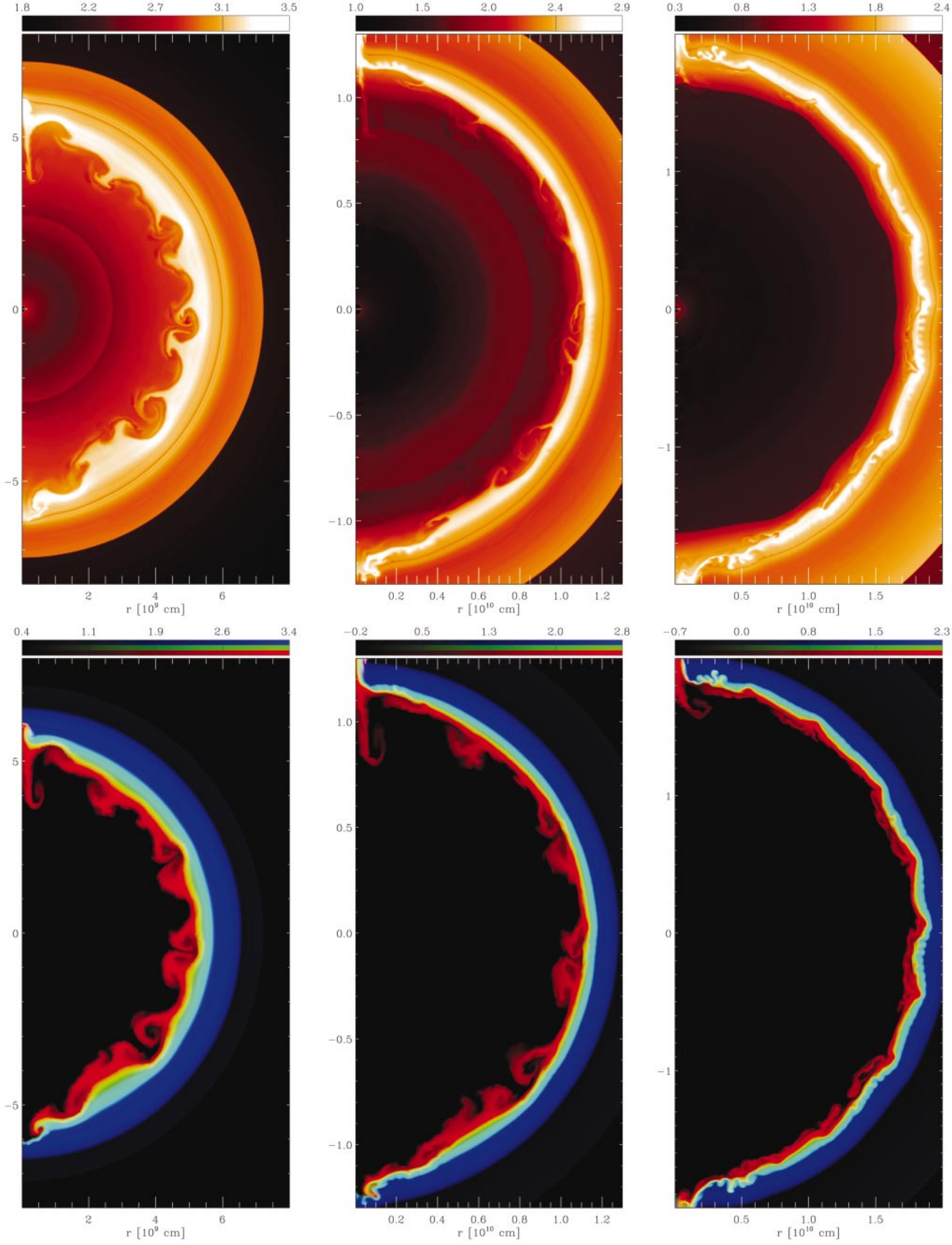

Fig. 12. Logarithm of the density (top) and of the partial densities (bottom) of ^{16}O (blue), ^{28}Si (green), and ^{56}Ni (red) in Model T310a at selected early epochs. Data values are coded according to the color bars given for each frame. In case of the partial densities, colors other than red, green and blue (resulting from the superposition of these color channels) indicate mixing of the composition. From left to right **a)** $t = 4$ s, **b)** $t = 10$ s, **c)** $t = 20$ s. Note the change of the radial scale. The supernova shock is visible as the outermost circular discontinuity in the density plots.

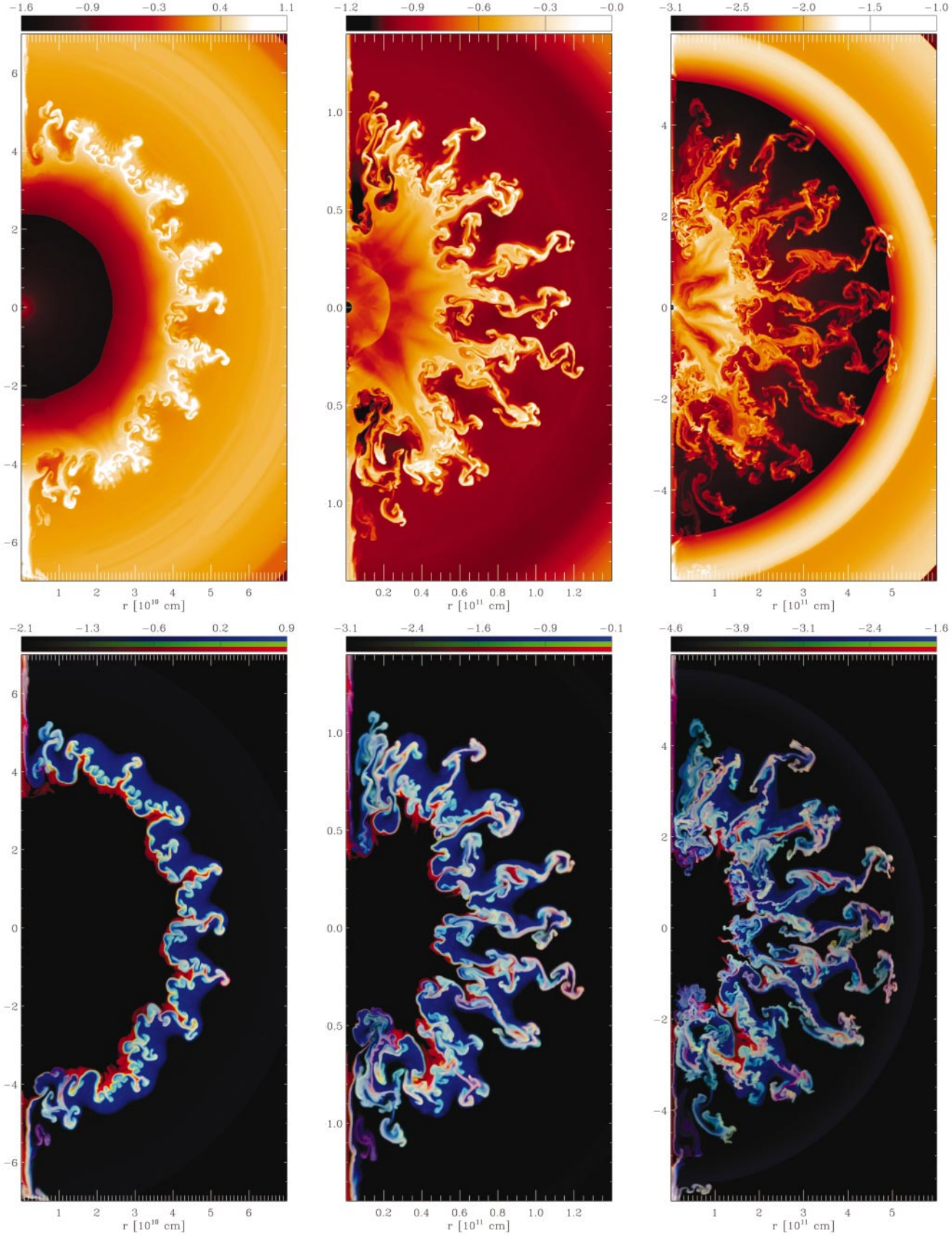

Fig. 13. Same as Fig. 12. **a)** $t = 100$ s (left), **b)** $t = 300$ s (middle), **c)** $t = 1500$ s (right). Note the change of the radial scale.

one-dimensional case, the density gradient at the inner edge of the shell steepens into a reverse shock. In the one-dimensional calculation, the layers of the metal core are well behind this reverse shock until $t = 2600$ s. Only then has the reverse shock propagated sufficiently deep inward in mass to reach the (C+O)/He interface (see also Kane et al. 2000 and Müller et al. 1991b). In our two-dimensional simulation, however, the fastest mushrooms already start to penetrate through the reverse shock at 1500 s after bounce (Fig. 13c). This interaction of the metal-enriched clumps with the reverse shock has not been pointed out in any previous study of Rayleigh-Taylor instabilities in type II supernova progenitors. It has important consequences for the velocity distribution of the elements because it leads to a strong deceleration of the clumps. We will address this issue in more detail below. For the moment we only note that after penetrating through the reverse shock and entering the high-density He-shell, the clumps move supersonically relative to the ambient medium. As a result they are dissipating a large fraction of their kinetic energy in bow shocks and strong acoustic waves. The wave fronts can be seen in Figs. 14a–c which show the interaction of the clumps with the shell between 5000 s and 20 000 s after bounce. Figure 14 also suggests that during this interaction the spatial distribution of the heavy elements inside the clumps is almost entirely homogenized. This causes the light blue and whitish regions in the abundance plots (lower panels of Figs. 14a–c) due to the superposition of the single colors that were assigned to the different elements. The interaction with the reverse shock also leads to mixing of ambient helium into the clumps, with the helium mass fraction becoming comparable to that of the heavy elements. Before, the clumps contained only small amounts of helium that was admixed to them during the first ∼300 s from the central zone of α-rich freezeout by the development of the Rayleigh-Taylor instabilities.

To facilitate a comparison of Model T310a with one-dimensional work, upon which most attempts to reproduce observations of nucleosynthetic yields and their distribution are based, we summarize the extent of mixing as a function of the enclosed mass in Fig. 15. The left panel shows the distribution of the mass fractions for the original presupernova model. At a time of 20 000 s after bounce (right panel), elements like ^{16}O and ^{28}Si, that made up the original metal core have been mixed almost homogeneously throughout the inner 3.4 $M_\odot$, along with the newly synthesized ^{56}Ni. The only nuclear species that are not mixed this far out in mass are the neutronization tracer and, to an even lesser extent, ^{44}Ti. These nuclei were synthesized in the innermost layers of the neutrino-heated ejecta very close to the collapsed core.

Note that the mixing is confined to the former He core of the star (i.e. the inner 4.2 $M_\odot$). This can be understood from Fig. 14: the dense He-shell, that forms just below the He/H interface, acts like an impenetrable wall for the metal clumps and shields the hydrogen envelope from becoming enriched with heavy elements. This result may appear somewhat surprising because, as we have shown by the linear stability analysis (Sect. 6.1), the He/H interface of the Woosley et al. (1988) star is Rayleigh-Taylor unstable. However, since we did not impose any seed perturbations in our AMR simulations and since the supernova shock is almost perfectly spherically symmetric when it crosses the He/H interface, the evolution of these layers proceeds initially one-dimensionally. This turns out to be true even in models where much more vigorous neutrino-driven convection imposes noticeable asphericities on the shock during its revival. Such asphericities, however, are smoothed out during the subsequent propagation of the shock through the helium core. The only deviations from spherical symmetry that perturb the He/H interface in Model T310a are the waves that are excited when the metal-enriched clumps hit the inner edge of the dense shell below the interface at times $t \geq 1500$ s. However, these perturbations encounter only a moderately unstable He/H interface at these late times, in accordance with the linear stability analysis (Fig. 11) which shows that after $t \sim 1500$ s the integrated growth rate, σ, increases only slightly. The mixing at the He/H interface is therefore rather weak. The instability at this interface has apparently evolved into the nonlinear regime by $t \approx 10\,000$ s, showing a multitude of small and somewhat bent fingers. However, these do not grow appreciably up to 20 000 s after bounce, when we stopped our 2D simulation. At this time the flow near the interface expands nearly self-similarly, i.e. the small fingers move with the same velocity as the medium between them. Note that the perturbations of the He/H interface that result from the accoustic waves are quite different from those used to initiate the instability in all previous studies. In the latter, seed perturbations of the order of 10% of the radial velocity were imposed on the entire star about 300 s after shock formation. With perturbations of this magnitude it is indeed possible to obtain strong mixing at the He/H interface of our progenitor. We have found such extended mixing in the late evolution of the hydrodynamic model discussed in Kifonidis et al. (2000), which suffered strongly from odd-even decoupling, and was therefore perturbed in the radial velocity by ∼20% at $t = 300$ s. However, even in this model the nickel was mixed out only to a mass coordinate of 4.5 $M_\odot$ after 10 000 s.

6.2.2. Clump propagation and velocity distribution of nucleosynthetic products

In Fig. 16 we show for times from 4 s until 20 000 s after bounce the logarithm of the fractional masses for several nuclei that are contained within the velocity interval $[v_\mathrm{r}, v_\mathrm{r} + \mathrm{d}v_\mathrm{r}]$ as a function of the radial velocity. Obviously, there occurs a bulk deceleration of the material from velocities as large as $\sim$14 000 km s^{-1} at a time of 4 s after bounce to $\sim$5000 km s^{-1} after 50 s. This is caused by the enormous deceleration that the shock and the post-shock material experience after the shock has entered the He core. The deceleration and the associated compression also cause the clear tendency of the mass distributions of the elements to narrow down in velocity space (Fig. 16).

Shortly before the shock crosses the (C+O)/He interface (i.e. for times 1 s $\leq t \leq$ 2 s) the abundance maxima of different elements are well-separated in radius. Together with the post-shock velocity gradient (Sect. 5.2) this results in maxima of the velocity distributions of different nuclei that are well-separated

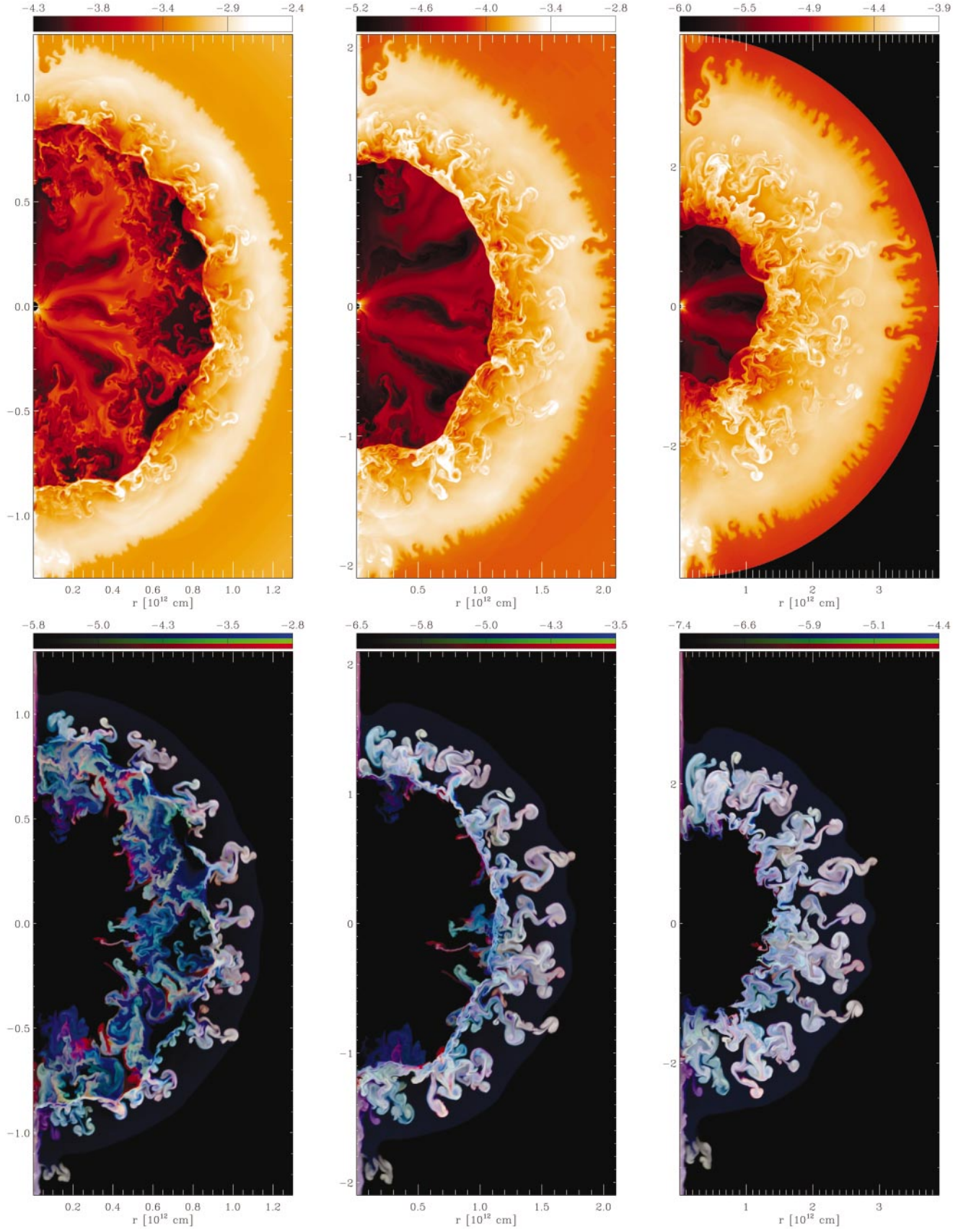

Fig. 14. Same as Fig. 12. **a)** $t = 5000$ s (left), **b)** $t = 10\,000$ s (middle), **c)** $t = 20\,000$ s (right). Note the change of the radial scale. The circular orange/black boundary in the upper right panel corresponds to the outer edge of the computational domain, which the supernova shock has crossed long before.

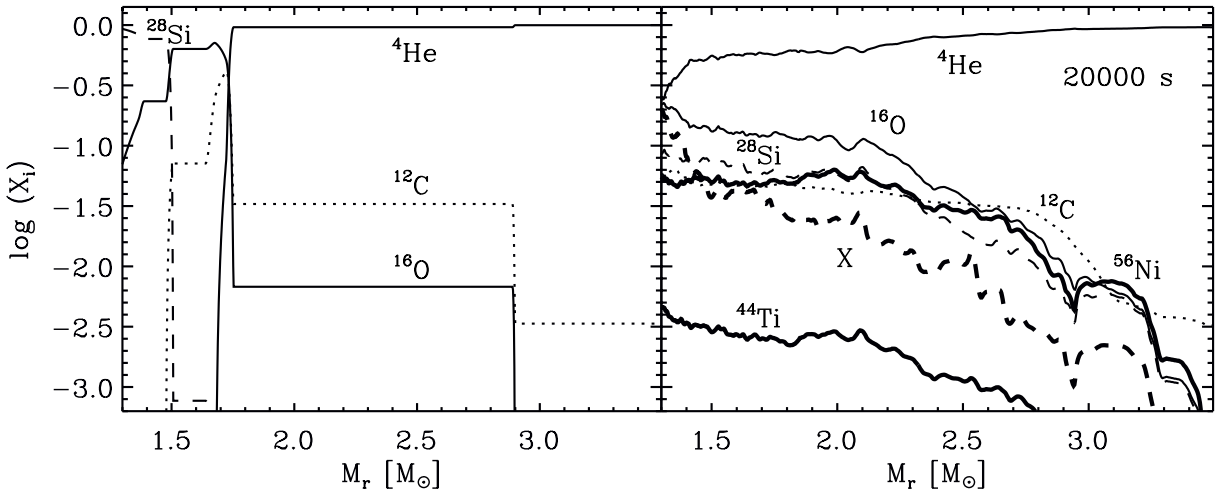

Fig. 15. Evolution of the extent of mixing in Model T310a. Left: initial composition. Right: composition 20 000 s after core bounce. The neutronization tracer is denoted with "X". Note that all heavy elements are confined to the helium core (i.e. to the innermost 4.2 $M_\odot$ of the star) even as late as 20 000 s after core bounce.

in velocity space. However, this separation disappears within the first 50 s after bounce due to the strong compression: being squeezed into a very dense shell, different nuclear species are getting very close in radius and thus they reflect the velocities that are prevailing in this shell. The first nuclei to become affected by the compression are ^{16}O, ^{28}Si and ^{56}Ni, since these are located closest to the supernova shock. A narrow peak forms in the velocity distribution of these elements already between 4 s and 10 s after bounce (Fig. 16). Being centered around 8500 km s^{-1} at t = 10 s, the peak gradually recedes to ∼3500 km s^{-1} at t = 50 s. The maximum velocities of ^{56}Ni and ^{28}Si are larger than this value by about 1500 km s^{-1}, while a small fraction of ^{16}O is found at somewhat larger velocities, still. Elements that are located closer to the inner boundary of the computational domain (i.e. ^{44}Ti and the neutronization tracer) show broader distributions in velocity space during the first ∼10 s of the explosion, until the strong compression also affects their spatial distribution and leads to a homogenization of all profiles in Fig. 16 around 50 s after bounce. This homogenization is actually fortunate for a comparison of our results to observational data, since it makes the late-time velocity distributions of nuclei in our models fairly robust against uncertainties that affect the nucleosynthesis in the neutrino-heated matter. In particular, the velocity profiles of ^{56}Ni and of the neutronization tracer nucleus are finally rather similar. Hence, it is not very relevant for the velocity distributions of these nuclei that nucleosynthesis in the inner ejecta depends on unknown details of the neutrino luminosities and spectra, which determine whether ^{56}Ni or mere neutron-rich nuclei are produced.

Up to a time of 300 s, when the Rayleigh-Taylor instabilities are still developing, the maximum velocity of ^{56}Ni is steadily decreasing, dropping to values of ∼3500 km s^{-1}. This maximum velocity is found in the mushroom caps of the Rayleigh-Taylor fingers. In the early stages of their existence these "clumps" have to propagate through a rather dense medium. In addition they "feel" the positive pressure gradient in the unstable layers. Hence they are decelerated appreciably, but less than the expansion of the surrounding matter is slowed down by this pressure gradient. Around 300 s, however, the density contrast between the clumps and their environment has grown substantially. In addition, at this time the sound speed is about 1400 km s^{-1} in the layers of the He core through which the clumps propagate, while the "background" flow is expanding with ∼3000 km s^{-1}. Comparing this to the clump velocity of 3500 km s^{-1} we find that at t = 300 s the clumps move relative to the He core with about 500 km s^{-1}, i.e. their motion relative to the background is *subsonic* and the drag they experience is rather small. As a result, the clumps "decouple" from the flow and start to move ballistically through the remaining part of the helium core, with the maximum ^{56}Ni velocity remaining roughly constant for times between 300 s and 1500 s. At approximately the latter time the clumps penetrate through the reverse shock at the inner edge of the dense shell that has formed below the He/H interface. After entering this shell they are strongly decelerated, and the maximum velocities of all elements drop to ∼1200 km s^{-1} as is visible for a time of 20 000 s after core bounce in Fig. 16. These values are significantly smaller than those observed in SN 1987 A. Note that prior to the interaction of the clumps with the shell, the nickel velocities of our models *are in accordance* with the velocities observed in SN 1987 A, i.e. a good match to the observations is prevented by the formation of the dense shell in the outer He core of our models. Several effects cause the strong slow-down of the clumps in the shell. They can be discussed by considering the expression for the drag force

$$F_{\rm D} = c_{\rm D}\frac{\rho v^2}{2}A, \qquad (4)$$

where A is the cross sectional area of a clump, ρ the ambient fluid density, v the velocity of the clumps relative to the ambient fluid, and $c_{\rm D}$ the drag coefficient. Since the clumps have to pass through a *reverse* shock they enter an environment with a *smaller* mean expansion velocity than in the layers upstream of the shock. Their velocity v relative to the new background is therefore *higher* than it was before they crossed the shock and amounts to $v \approx 1300$ km s^{-1} at t = 1500 s. In addition ρ is

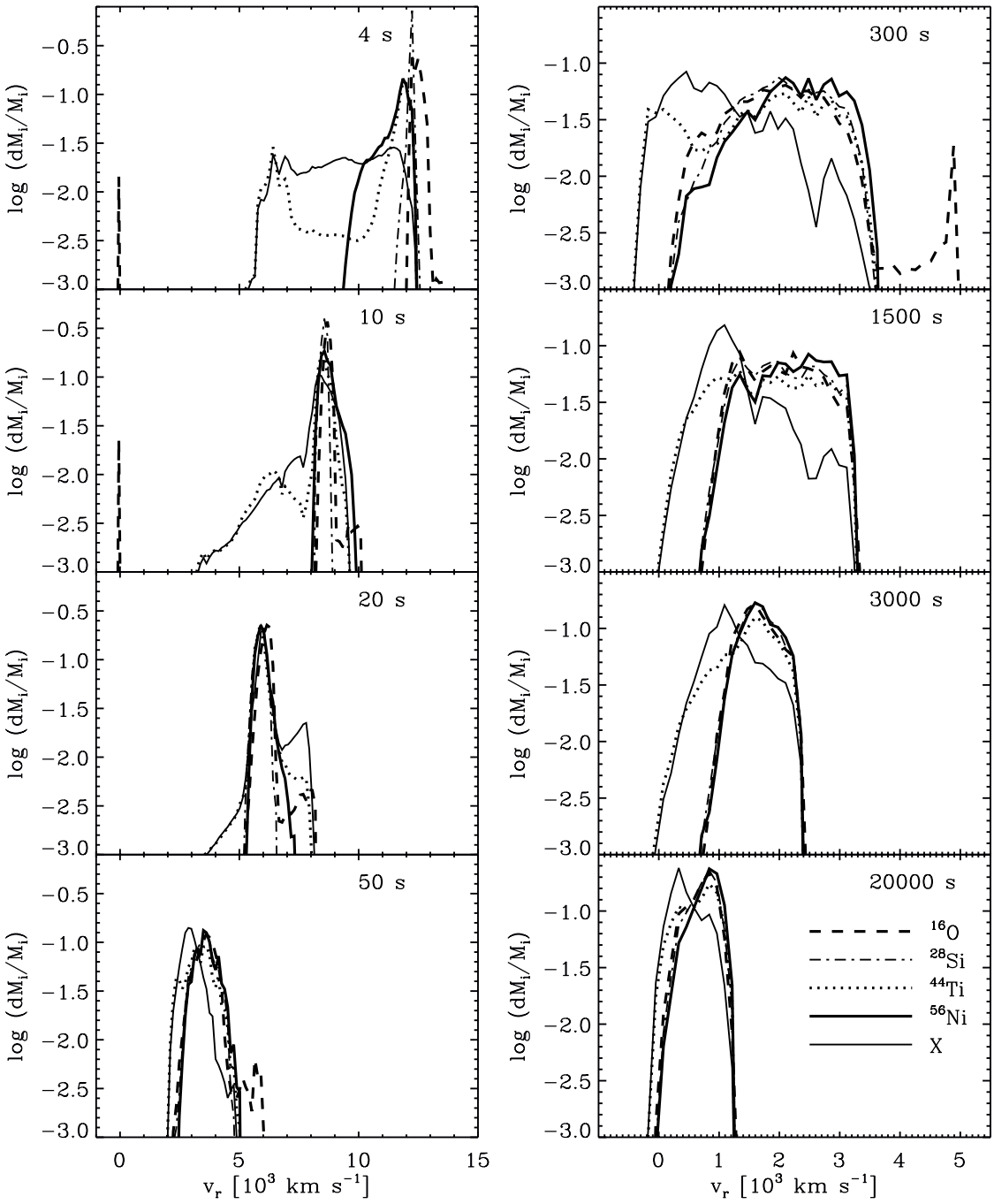

Fig. 16. Logarithm of the fractional mass of different elements that is contained within the velocity interval $[v_r, v_r + dv_r]$ as a function of the radial velocity v_r in Model T310a at various epochs. The resolution is $dv_r \approx 130\,\mathrm{km\,s^{-1}}$. Note the different scales for the radial velocity in the left and right panels.

larger in the post-shock region. Both effects increase the drag by increasing the ram pressure ρv^2. The sound speed in the post-shock layers is rather small ($890\,\mathrm{km\,s^{-1}}$) at $t = 1500\,\mathrm{s}$. Therefore, the clumps move *supersonically* through the dense medium, with Mach numbers $M \approx 1.5$. The drag coefficient c_D of a projectile increases steeply in the subsonic/supersonic transition (this is the well-known "sound barrier"). The effect is even more pronounced if the projectile's shape is roundish (as in the case considered here) and not pointed. Together with the increase in ram pressure, the supersonic motion leads to a large rise of F_D, and hence to significant energy dissipation.

The interaction of the clumps with the reverse shock resembles the well-studied problem of a (planar) shock interacting with an overdense, spherical, interstellar cloud that is in pressure equilibrium with its surroundings (see Klein et al. 1994, and the references therein). In this case it has been shown that the interaction can be divided into four stages. In the first phase, the blast wave strikes the cloud driving a shock into

the cloud and a reflected shock into the (shocked) intercloud medium. The reflected shocks resulting from this phase correspond to the bow-shocks that we observe and which pervade the entire dense helium shell in our simulation between 3000 s and 20 000 s after bounce (Sect. 6.2.1). In the second stage the cloud is compressed into a pancake-like structure. Indications of this phenomenon can be seen in Fig. 13c. The third stage is the reexpansion phase in which the cloud expands laterally. This increases its cross section, A, and thus hastens its deceleration (see Figs. 14a–c). In the fourth and final phase the cloud is destroyed by vorticity generation due to the development of Rayleigh-Taylor and Kelvin-Helmholtz instabilities at its surface. We do not observe a complete disintegration of the metal clumps according to this last phase in our simulations. It is not clear, whether this is due to numerical reasons, due to the fact that we might have simply stopped our simulations too early for the instabilities to grow appreciably, or due to differences in the physics of both problems. In our case the density contrast between a clump and the medium upstream as well as downstream of the reverse shock (the former quantity is a constant in Klein et al. 1994) is time-dependent, because the overall expansion decreases the densities. Furthermore, our reverse shock has a Mach number $M \sim 1$ and is thus not very strong, in contrast to the shocks studied by Klein et al. (1994), for which $M \gg 1$. In addition, the mushroom caps of our Rayleigh-Taylor fingers have typical radii $r_{\rm clump} \sim 0.1 R_{\rm s}$, with $R_{\rm s}$ being the radius of the reverse shock. Thus they do not satisfy the small clump criterion ($r_{\rm clump} \leq 0.01 R_{\rm s}$) that Klein et al. (1994) assumed for their study. Finally, our problem has a more complicated geometry and equation of state. Recent experiments of $M \sim 1$ shocks in air interacting with a cylindrical column of high-density gas (Fishbine 2002; Zoldi 2002) indicate that the gas column is strongly ablated, developing significant vorticity at its edges. However, it is not entirely destroyed.

Klein et al. (1994) report that for the shock-cloud interaction problem, about 120 zones per cloud radius are required to reduce numerical viscosity in a second-order Godunov-type hydrodynamic scheme to the point that converged results can be obtained. With ∼20 zones per clump radius our resolution is much lower. Resolution studies are required in order to decide whether our velocity distributions are numerically converged. The same holds for answering the question whether the clumps will get dispersed and mixed with the material of the "helium wall", or whether they can survive as individual entities. Note also that in the end 3D calculations will be required since the drag coefficient, $c_{\rm D}$, and the cross section, A, in Eq. (4) depend on clump shape, which can lead to quantitative differences in three-dimensional as compared to our two-dimensional simulations. The Rayleigh-Taylor fingers that one finds in a two-dimensional calculation are comparable to genuine 3D "mushrooms" only along the polar axis of the 2D grid. Along the equator one actually obtains toroidal structures because of the assumption of axial symmetry (see Kane et al. 2000, and the references therein). Judging from the 2D results of Klein et al. (1994) and the 3D calculations of Stone & Norman (1992) for the shock-cloud interaction problem, we have little doubt, however, that independent of the dimensionality of the calculation the metals must slow down appreciably. We consider this to be a potentially serious problem for obtaining high velocities for the metals in the H-envelopes of type II supernova models. Efficient re-acceleration mechanisms operating at later phases of the evolution are currently unknown.

Actually there is no physical reason to expect an acceleration of matter (relative to the observer's frame) by the instabilities. The pressure gradient in the Rayleigh-Taylor unstable layers of the ejecta is *positive*, i.e. these layers are *decelerated*. In fact it is this deceleration that leads to the formation of Rayleigh-Taylor fingers: Since overdense parcels of gas have a larger momentum than the neighbouring material, they *cannot be slowed down as efficiently* as the surrounding matter and hence they start to move outward relative to their ambient medium. During no time, however, the clumps are accelerated with respect to the observer's rest frame. The reason why we obtain high ^{56}Ni velocities in the early evolution of our models is the fact that the nickel clumps decouple from the (continuously decelerated) background flow and subsequently move ballistically through the ejecta. By decoupling from the background, the clumps can nearly conserve their high initial velocity beyond the time of decoupling and thus move outward in mass until they become comoving with the outer ejecta. It must be noted, though, that these high initial ^{56}Ni velocities are only obtained if clump formation starts sufficiently early, i.e. within the first ∼10 s after bounce, when the velocity in the ^{56}Ni-rich layers is still high (compare Fig. 9a). If clump formation is delayed by a few 100 s, the ^{56}Ni velocities have already dropped to values $<1500\,{\rm km\,s^{-1}}$ (Fig. 9b) and it becomes impossible to obtain high velocities by "clump decoupling" during the subsequent evolution. This is the reason why earlier investigations of Rayleigh-Taylor mixing in type II supernovae, which started from one-dimensional models 300 s after bounce, obtained only low ^{56}Ni velocities. The only exception were some of the SPH calculations of Herant & Benz (1992) which showed nickel velocities of $\sim 3000\,{\rm km\,s^{-1}}$. As stated by the authors, this result is a direct consequence of an assumed premixing of ^{56}Ni throughout 75% of the metal core of the 1D explosion model of a $20\,M_{\odot}$ progenitor, from which they started their 2D calculations at $t = 300$ s. In contrast to their approach, in which this (early) mixing was put in by hand, we have attempted to perform consistent and continuous high-resolution 2D simulations of the entire shock propagation through the star. Doing so, we find that even if one succeeds to obtain high metal velocities during the first minutes of the explosion, there is no guarantee that these velocities will remain high throughout the later evolution. As we discussed earlier, a main obstacle to overcome is the interaction of the metal clumps with the reverse shock below the He/H interface, which dramatically reduces the nickel velocities in our simulations. It is not clear to us why this nickel deceleration is not present in the models of Herant & Benz.

Herant & Benz (1992) reported that the energy release due to the radioactive decay of ^{56}Ni and ^{56}Co is inefficient to significantly boost the nickel velocities over the first few months. However, further studies of this effect, which should start from models like ours and use more accurate hydrodynamic schemes and higher resolution than the calculations of Herant & Benz (1992) are clearly required. At present, we have to conclude

that high final clump velocities can only be obtained if the clumps decouple sufficiently early from the background flow, and if the helium wall and the associated reverse shock do not form. The latter requires that the main shock does not decelerate in the hydrogen envelope, i.e. the density gradient outside the He core has to be steeper than $\propto r^{-3}$. A situation where this might hold is the case of a type Ib supernova explosion. The progenitors of type Ib supernovae are thought to be stripped He cores that lack a thick hydrogen envelope. In this case the shock directly enters the tenuous atmosphere of the star once it leaves the dense part of the He-rich layers.

7. Beyond the first second: A type Ib model?

To confirm the effect of a steeper density decline upon clump propagation we have removed the outer envelope of our progenitor model and replaced it by power-law profiles for the density and temperature of the form

$$\rho(r) = \rho_c \frac{r_c^n}{r^n}, \tag{5}$$

$$T(r) = T_c \frac{r_c^m}{r^m}, \quad \text{for } r \geq r_c. \tag{6}$$

Herein r_c is the radius at which the original model was cut, ρ_c and T_c are the density and temperature at that radius, and $n = 4.25$ and $m = 1.32$ are the adopted power-law indices for the density and temperature profiles, respectively. We have chosen $r_c = 5.0 \times 10^{10}$ cm, i.e. we placed the cut still inside the He core at a mass coordinate $M_r = 3.89\,M_\odot$, while the mass of the new envelope amounted to $1.2\,M_\odot$. Note that this simple setup of a "type Ib progenitor" lacks internal consistency. It does not take into account that mass-loss due to winds (or binary interaction) will gradually alter the entire structure of the star during its evolution and that the density profile at the onset of core collapse obtained from a consistent stellar evolutionary calculation will therefore look different from our model. For this reason the calculations discussed below can only demonstrate effects in principle, and the simulations should be repeated with generic type Ib progenitors (e.g. Woosley et al. 1995) to discuss observationally relevant aspects in detail. In the context of the present work we refrained from doing so but wished to start with our explosion model T310 as described in Sect. 5.2, and follow clump propagation in our truncated progenitor with AMRA until 3000 s after bounce. At this epoch the expansion is already self-similar, i.e. the clumps are "frozen in" and move with the same velocity as the ambient medium.

The simulation in this section, to which we will henceforth refer to as Model T310b, was performed with a maximum resolution of 1536 × 384 zones. Otherwise we used the same computational strategy as for Model T310a of Sect. 6.2. Not surprisingly, the evolution in Model T310b proceeded identically to the previous type II supernova model, T310a, for the first 50 s, i.e. the time it took the shock to reach the mass coordinate where we truncated the original progenitor and where the density in the modified model now starts to decline steeply. It is remarkable, however, that the velocity profiles for all chemical elements show only minor differences between Model T310b (Fig. 17) and Model T310a (compare Fig. 16) even as late as 300 s after bounce. This also indicates that the lower resolution used in Model T310b has only small effects on the overall dynamics. However, it suppresses smale-scale fragmentation due to Kelvin-Helmholtz instabilities which is visible in Fig. 13c but not in Fig. 18. Significant differences between both cases start to develop only for times later than 300 s. As we expected, the formation of a reverse shock and an associated dense helium shell is absent in the outer core of Model T310b (compare Fig. 18 with Fig. 13c). Instead of suffering from a deceleration in such a dense environment the metal clumps can now expand freely into a tenuous medium, i.e. the velocity profiles of all chemical elements do not change any more after 300 s (Fig. 17). Maximum velocities of 3500 km s^{-1} are obtained for ^{28}Si, ^{56}Ni, ^{44}Ti, and for the neutronization tracer, while ^{16}O expands with velocities as high as 5500 km s^{-1}.

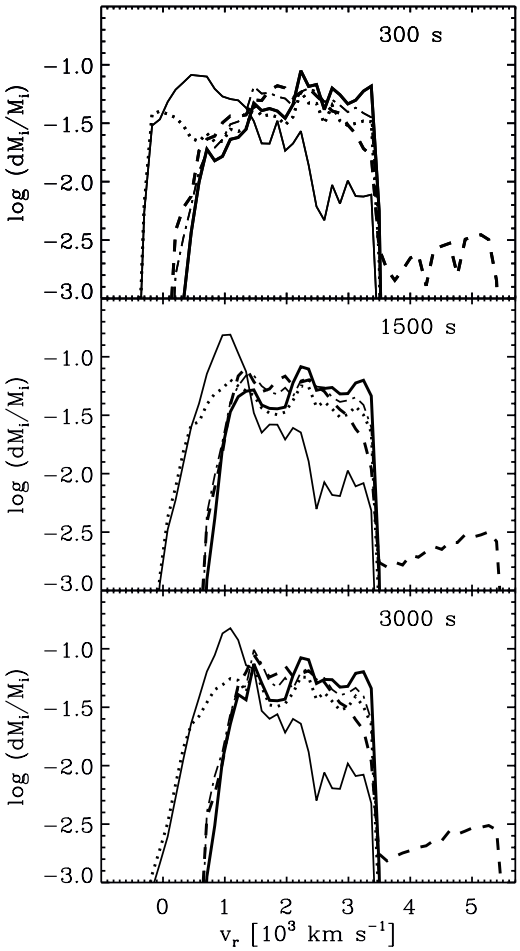

Fig. 17. Same as Fig. 16 but for Model T310b and times of 300 s, 1500 s and 3000 s after bounce.

Figure 19 displays the extent of the mixing (averaged over angle) for this model at a time of 3000 s. The newly synthesized nuclei are mixed throughout the inner $2.0\,M_\odot$ of the star. Figure 19 should be compared to the plots of "Model 4B" of Woosley & Eastman (1997), who computed synthetic spectra from one-dimensional explosion models of a $2.3\,M_\odot$ He core (originating from a $4\,M_\odot$ He star) and demonstrated that very good agreement with observed spectra of SN 1984 L near maximum light could be achieved. This was only the case,

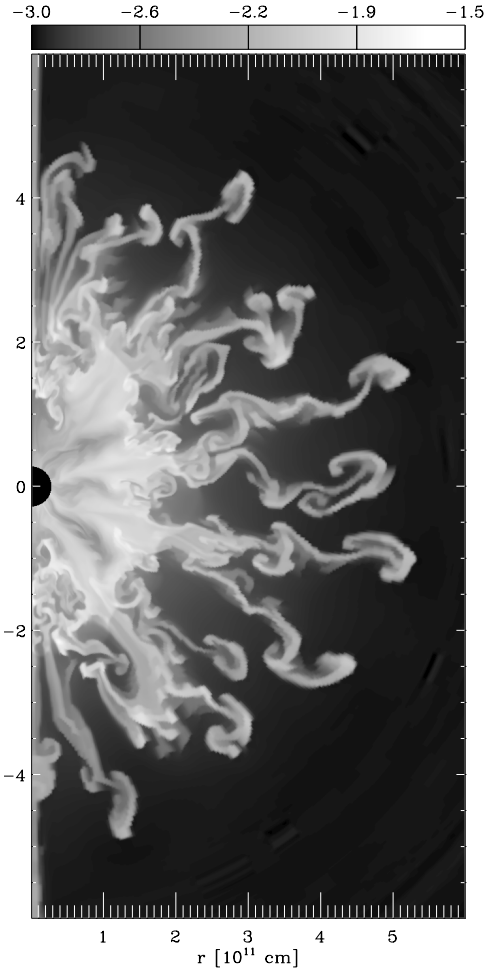

Fig. 18. Logarithm of the density in Model T310b at a time of 1500 s after bounce.

however, if they artificially mixed ^{56}Ni into the helium rich layers assuming an exponential decline of the ^{56}Ni mass fraction, $X(^{56}\mathrm{Ni})$, with the enclosed mass. The value of $X(^{56}\mathrm{Ni})$ decreased below 10^{-3} only at a mass coordinate of $\sim 2\,M_\odot$. Different from Model 4B of Woosley & Eastman (1997) our Model T310b (Fig. 19) shows a plateau-like distribution with high nickel mass fractions ($\log X(^{56}\mathrm{Ni}) \approx -1.0$) up to the outer edge of the nickel-enriched core. The latter coincides with that of the Woosley & Eastman model. Whether this is sufficient to cause an adequately large flux of ionizing γ-photons in the He envelope in case of our more massive star ($5.1\,M_\odot$ instead of $2.3\,M_\odot$ for Woosley & Eastman's "Model 4B") can only be decided by calculating detailed spectra. Our purpose here is only to demonstrate that multi-dimensional hydrodynamic models, with a consistent treatment of the early phases of the explosion, can yield strong mixing of the metal and He core that is a prerequisite to produce a good match between calculated and observed spectra and light curves of type Ib supernovae (Shigeyama et al. 1990; Hachisu et al. 1994; Woosley & Eastman 1997). Hachisu et al. (1994) have shown that in order to obtain a sufficient amount of mixing in multi-dimensional simulations with artificially triggered Rayleigh-Taylor instabilities, the amplitude of the seed perturbations must exceed 5% of the radial expansion velocity at the time the shock crosses the unstable interfaces in the metal core. Our models demonstrate that such a degree of perturbation can be naturally obtained as a result of neutrino-driven convection during the first second of the explosion.

A most remarkable feature of Model T310b is the fact that the number of Rayleigh-Taylor fingers at times $t \geq 1500$ s is correlated with (indeed it is essentially equal to) the number of down-flows that developed in the convective layer of neutrino heating behind the shock (compare Fig. 18 to Fig. 1b). This correlation, although initially present, is destroyed in Model T310a, where the interaction of the clumps with the reverse shock and the dense helium shell results in a stronger non-linear evolution with substantial vorticity generation and mixing. As the structure of down-flows and neutrino-heated bubbles characterizes the mode of the convective pattern that prevails within the shock-revival phase, it carries important information about the mechanism that initiates the explosion. It would be interesting if our finding is generic, and if it also holds for cases where the pattern of neutrino-driven convection develops much larger modes than those obtained in our simulations. At present, however, one must be cautious not to overinterpret our result, which is based on a single 2D model. A confirmation of the existence of a tight correlation between the patterns of the early post-shock convection and the final instabilities in the mantle of the exploding star will probably require well-resolved 3D calculations and parameter studies with different explosion and progenitor models.

8. Conclusions

We have presented a study of hydrodynamic instabilities in a type II and a type Ib-like supernova model that has improved upon earlier simulations by starting the explosion by means of neutrino heating behind the stalled supernova shock and by following the hydrodynamics of this explosion well beyond shock-breakout from the stellar photosphere. The consistency of the hydrodynamic evolution that was thereby achieved allows for the following conclusions.

- We find newly synthesized ^{56}Ni and the products of incomplete silicon and oxygen burning to be initially located in a high-density (low entropy) inhomogeneous shell that forms behind the outward sweeping shock within the first $\sim$500 ms of the evolution. Depending on the explosion time scale and the strength of the neutrino-driven convection this shell is either markedly or weakly deformed by rising, high-entropy bubbles of neutrino-heated matter. The angular extent of these bubbles is larger for long explosion time scales (usually leading to smaller explosion energies of our progenitor) and large seed perturbations. Besides being formed by Si-burning ^{56}Ni is also produced in significant amounts in the neutrino-heated high-entropy bubbles if their neutronization is moderate. The latter is sensitive to the ν_e and $\bar{\nu}_\mathrm{e}$ luminosities and spectra imposed at the inner boundary in our simulations.
- The outer boundary of the ^{56}Ni-rich shell is located close to the Si/O composition interface where a negative density

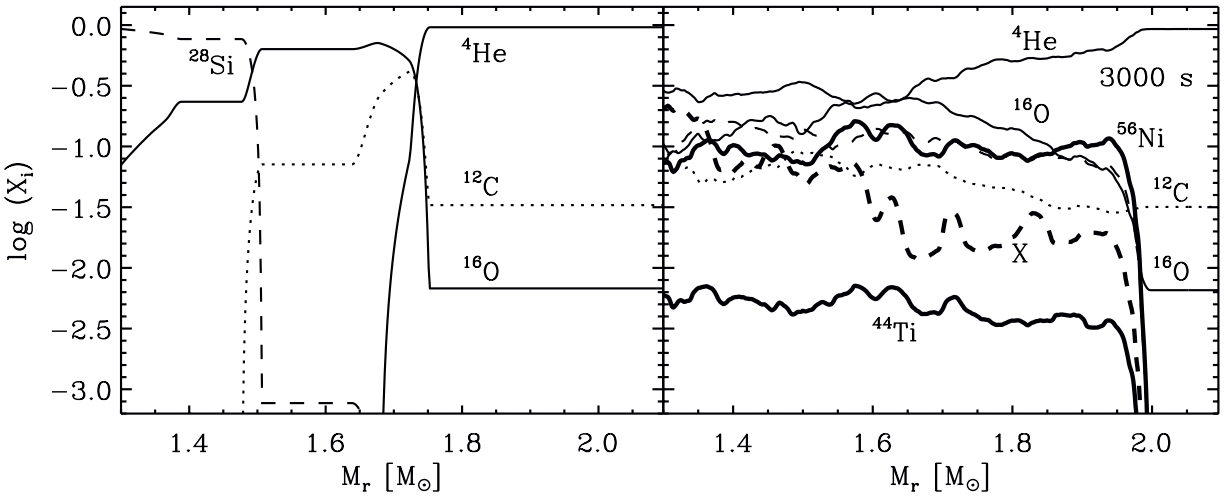

Fig. 19. Same as Fig. 15, but for Model T310b. Left: initial composition. Right: composition 3000 s after core bounce.

and a positive pressure gradient exist. This state is unstable to the Rayleigh-Taylor instability.

- For an explosion energy around 1.8×10^{51} ergs, ^{56}Ni is born with velocities $\leq$17 000 km s^{-1}. These velocities are much larger than those typically observed for the metal clumps in supernovae, and indicate that a substantial deceleration of this material must occur when it penetrates through the overlying layers of the star.
- Three Rayleigh-Taylor unstable regions develop in the explosion of the 15 $M_\odot$ progenitor model of Woosley et al. (1988): one at the Si/O interface, a second one at the (C+O)/He interface and a third one at the He/H interface of the star.
- Seeded by the perturbations induced by neutrino-driven convection, Rayleigh-Taylor mixing at the Si/O interface sets in already about 20 s after core bounce and leads to a fragmentation of the ^{56}Ni-enriched shell with the formation of fingers that distort also the (C+O)/He interface farther out.
- Within only about five minutes after bounce the entire metal core of the Woosley et al. (1988) star is shredded.
- Dense "bullets" and clumps of ^{56}Ni, ^{28}Si and ^{16}O-rich material decouple from the flow and start to propagate ballistically through the stellar helium core.
- During this phase, metal velocities as high as 3500–5500 km s^{-1} are observed, and the pattern of the Rayleigh-Taylor structures carries information about the geometry of the neutrino-driven convection from the shock-revival phase.

The effects discussed above could not be seen in previous studies of Rayleigh-Taylor instabilities in core collapse supernovae where the explosion was started by ad hoc energy deposition (using pistons or thermal bombs). Especially the high ^{56}Ni velocities, the strong mixing triggered at the Si/O interface, and the very short growth time-scale of the instabilities at the Si/O and (C+O)/He interfaces (minutes as compared to hours) are in clear contrast to what has been reported in previous studies, especially in those which dealt with the mixing in type II supernovae. Of all earlier works, only the type Ib studies of Hachisu et al. (1994) and the SN 1993 J simulations of Iwamoto et al. (1997) agree qualitatively with the evolution that we observe for the first minutes of the explosion. Both of these studies found, as we do, that Rayleigh-Taylor instabilities at the (C+O)/He interface of the progenitor stars grow within minutes after core collapse. However, they did not observe the instability at the Si/O interface. Moreover, they had to assume large seed perturbations to induce the mixing, whereas in our case the perturbations are a natural consequence of neutrino-driven convection.

The crucial difference between our type II model T310a and all other type II supernova simulations (except for the work of Iwamoto et al. 1997) is the fact that our metal core starts to fragment within only about 20 s after bounce, when the velocity in the ^{56}Ni-rich layers is still high (see Fig. 9a). This leads to an early decoupling of the clumps from the background flow, enabling the clumps to conserve the high velocity that the flow possesses at early times. Not allowing for early clump formation and decoupling, as it has been done in nearly all previous multi-dimensional simulations of type II supernovae by starting the calculations hundreds of seconds after core bounce from 1D initial models, has the effect that the velocities of the ^{56}Ni-rich layers have dropped to values $\leq$1500 km s^{-1} at the start of the multi-dimensional calculation (Fig. 9b). It therefore becomes impossible to obtain high velocities by the Rayleigh-Taylor instabilities during the subsequent evolution.

In fact, the situation becomes even worse at later times. We find that our Model T310a is initially successful in yielding high ^{56}Ni velocities: once the ^{56}Ni clumps in this model have decoupled from the flow, they propagate ballistically and subsonically through the helium core. Due to their subsonic motion, they do not dissipate much of their kinetic energy and the maximum ^{56}Ni velocities remain high at 3500 km s^{-1}. However, this changes when the clumps reach the outer helium core and encounter the reverse shock and the dense (Rayleigh-Taylor unstable) "wall" that are left behind by the main shock below the He/H interface. When the clumps penetrate through the reverse shock into this wall, 1500 s after core bounce, they are decelerated due to supersonic drag to

velocities $<1500\,\mathrm{km\,s^{-1}}$. An interaction of the clumps with the reverse shock is also present in data of previous type II supernova simulations (Müller et al. 1991b,a). However, its importance for clump propagation was not recognized because

- due to the late phase when previous multi-dimensional calculations were started, clump formation at the (C+O)/He interface was only about to set in at $t \approx 2000\,\mathrm{s}$, when the reverse shock had propagated sufficiently far inward in mass to reach this interface,
- the initial clump velocities and the densities in the shell downstream of the reverse shock were low, leading to less pronounced effects during the interaction,
- and the employed numerical resolution was insufficient to resolve the non-linear waves that characterize this interaction.

A final difference between Model T310a and previous type II supernova simulations is the fact that we do not obtain strong mixing at the He/H interface. Unless we add artificial perturbations to these layers, as it was done in all previous studies, the mixing remains very weak. This might indicate that neutrino-driven convection is not able to provide perturbations that are sufficiently strong to cause the large-scale mixing that was observed in SN 1987 A. However, final conclusions regarding this point are not possible before Rayleigh-Taylor simulations have been performed which start from a globally aspherical situation, as seen in recent calculations of neutrino-driven explosions (Janka et al. 2003; Scheck et al., in preparation).

Taken together, the effects revealed by our simulations demonstrate that the evolution proceeds multi-dimensionally from the earliest moments. Convective instabilities during the shock-revival phase cannot be neglected. They lead to very early growth of Rayleigh-Taylor instabilities and thus to high initial clump velocities what in turn determines the character of the late-time hydrodynamic evolution. By starting from 1D initial models hundreds of seconds after core bounce, all earlier investigations of Rayleigh-Taylor mixing in type II supernovae have therefore missed essential parts of the physics of the problem.

Supernova 1987 A still remains an enigma, though. Given the (late) deceleration of the clumps below the He/H interface in Model T310a, we wonder whether the conflicting maximum ^{56}Ni velocities between our models and the observations point to deficiencies of the "standard" blue supergiant progenitors, or to missing physics in our shock-revival simulations. There are indications that the progenitor of SN 1987 A might have been the result of a merger of two smaller stars (Podsiadlowski 1992) and that therefore its structure might not be accounted for reliably by "standard" stellar evolutionary calculations. Numerical studies of such mergers have recently been performed by Ivanova et al. (2002). Although their models show density profiles in the hydrogen envelope that look similar to the one of our progenitor (N. Ivanova, private communication), it remains to be seen in future simulations whether for these models the evolution differs from what we have reported here.

Sources of uncertainty in our calculations that may affect the velocities of chemical elements are the still limited numerical resolution and especially the differences between two-dimensional versus three-dimensional hydrodynamics. The smaller drag that clumps experience in three dimensions (Kane et al. 2000) may lead to higher initial clump velocities after the fragmentation of the metal core and thus to a farther penetration of the clumps through the helium "wall". This might result in higher final ^{56}Ni velocities than in two dimensions. An extension of our calculations to three dimensions with a similar resolution as in the 2D case appears hardly feasible in view of present computer resources. Further insight might, however, be gained by laser experiments (Robey et al. 2001; Kane et al. 2001; Drake et al. 2002; Klein et al. 2003, and the references therein), and hydrodynamic code validation experiments as those described by Fishbine (2002) and Zoldi (2002) before well-resolved 3D hydrodynamic simulations will become available.

There has been much speculation about large-scale anisotropies caused by jets in the explosion of SN 1987 A (Khokhlov et al. 1999; Wheeler et al. 2002; Wang et al. 2002). However, convincing and consistent (MHD) calculations of the formation and propagation of such jets and an associated explosion have not yet been performed. It is unclear whether in this scenario nickel velocities can be obtained that are in agreement with those observed in SN 1987 A. An initial anisotropy of the explosion, that might lead to high initial nickel velocities, would have to work against the same effects in the envelope that we find to be important in our simulations. The interaction with the reverse shock and the dense helium shell might not only slow down fast metal clumps, it might also reduce an initial anisotropy of the ejecta. Judging from the experience gained from our calculations, we doubt that the spatial resolution in simulations of anisotropic explosions that have been performed to date (Nagataki et al. 1997, 1998; Khokhlov et al. 1999) was sufficient to study these effects reliably. The origin of the prolate deformation of the ejecta of SN 1987 A (Wang et al. 2002) must therefore be regarded to be unknown. In fact, there is currently neither observational nor theoretical evidence that unambiguously demands the assumption of a "jet-driven" explosion. The deformation could as well be linked to an anisotropic initiation of the explosion due to neutrino heating (Janka et al. 2003; Plewa et al., in preparation). On the other hand it might also be caused by stellar rotation as a result of a merger history of the progenitor.

While clearly substantial work is required in case of SN 1987 A, our "type Ib" Model T310b is in reasonably good agreement with observations of extragalactic type Ib supernovae. Due to the absence of dense shell and reverse shock formation in the He core of this model, the metal-rich clumps are not decelerated once they start to propagate ballistically through the ambient gas and the final metal velocities of $3500-5500\,\mathrm{km\,s^{-1}}$ are sufficiently high. In addition, the extent of the mixing in this model is comparable to what Woosley & Eastman (1997) had to assume in their "Model 4B" to model the spectrum of SN 1984 L. This result is very encouraging. It indicates that the interaction of neutrino-driven convection with the Rayleigh-Taylor instabilities in the stellar mantle is able to account for important aspects of the mixing of different

elements in type Ib supernovae which are known from spectral and light curve calculations for more than a decade.

Another interesting aspect of Model T310b is the fact that without the strong non-linear interaction of the clumps with the reverse shock, perturbations originating from the shock-revival phase are reflected in the final flow structures of the Rayleigh-Taylor instabilities. This may enable one to deduce information about the pattern of the neutrino-driven convection from observations of the distribution of metals in the ejecta of type Ib supernovae. The possibility to obtain such a unique piece of evidence from ejecta properties is exciting. However, before such conclusions can be drawn, our results need to be ascertained by making use of a larger number of shock-revival simulations with different properties and a greater range of (type Ib and type Ic) progenitors. We believe that in the end very well-resolved 3D simulations will be required to prove the existence of such a correlation. If confirmed it might provide us with a means to probe the physics linked to the explosion mechanism even for extragalactic supernovae.

Finally, we emphasize that clump deceleration due to the interaction with the reverse shock might be crucial for a correct interpretation of observations of the different supernova types. It can cause different final metal clump velocities even if the initiation of the explosion proceeds similarly in different stars. The latter must actually be expected for the neutrino-heating mechanism, because the post bounce models of supernova cores are rather similar, regardless of whether they originate from type II or type Ib progenitors (Rampp et al., in preparation). On the other hand, clump deceleration depends on the structure of the envelope of the progenitor and a sequence is conceivable where its importance varies with the type of the supernova, being strongest in (some fraction of?) type II events and weaker or absent in type Ib and Ic supernovae. Unfortunately, observational data of metal clump velocities are currently sparse and hence they do not allow one to test this hypothesis. Photospheric velocities, as those published recently by Hamuy (2003), are not very helpful in this respect because they only probe the outer, faster expanding layers of the ejecta. To enlarge the data base recourse must be made to measurements of velocities in supernova remnants. Clumps moving with up to $\sim 6000\,\mathrm{km\,s^{-1}}$ were, however, observed in Cas A (van den Bergh 1971; Thorstensen et al. 2001), which is probably the remnant of a type Ib explosion (Fesen & Becker 1991), and clump velocities of up to $\sim 6000\,\mathrm{km\,s^{-1}}$ and $\sim 4000\,\mathrm{km\,s^{-1}}$ were measured shortly after the explosion in the type Ib SN 1987 F (Filippenko & Sargent 1989) and the type IIb SN 1993 J (Spyromilio 1994), respectively. All of these objects are assumed to be connected to progenitors with small or lacking hydrogen envelopes. On the other hand Aschenbach (2002) and Aschenbach et al. (1995) deduce low mean expansion velocities of about $2000\,\mathrm{km\,s^{-1}}$ for the clumps in the Vela supernova remnant (using their angular distance to the pulsar, the age of the latter and the distance of the remnant), that are in reasonably good agreement with our type II Model T310a. In fact, the Vela clumps show Mach cones and appear to move at present as slow as $\sim 500\,\mathrm{km\,s^{-1}}$ (Aschenbach 2002; Aschenbach et al. 1995), indicating that supersonic drag plays an important role even in the supernova remnant phase.

Acknowledgements. We thank S. E. Woosley and S. Bruenn for providing us with the progenitor and post-bounce models, respectively, that we have used to construct our initial data, and our referee, C. Fryer, for his comments on the manuscript. KK and HTJ are grateful for support by the Sonderforschungsbereich 375 on “Astroparticle Physics” of the Deutsche Forschungsgemeinschaft. The work of TP was supported in part by the US Department of Energy under Grant No. B341495 to the Center of Astrophysical Thermonuclear Flashes at the University of Chicago, and in part by grant 2.P03D.014.19 from the Polish Committee for Scientific Research. The simulations were performed on the CRAY J916, NEC SX-4B and NEC SX-5/3C computers of the Rechenzentrum Garching, and on the IBM Night Hawk II of the Max-Planck-Institut für Astrophysik.

References

Arnett, W. D., Bahcall, J. N., Kirshner, R. P., & Woosley, S. E. 1989a, ARA&A, 27, 629
Arnett, W. D., Fryxell, B., & Müller, E. 1989b, ApJ, 341, L63
Aschenbach, B. 2002, in Neutron Stars, Pulsars, and Supernova Remnants, Proc. of the 270th WE-Heraeus Seminar, ed. W. Becker, H. Lesch, & J. Trümper (Garching: Max-Planck-Institut für extraterrestrische Physik), 13
Aschenbach, B., Egger, R., & Trümper, J. 1995, Nature, 373, 587
Berger, M. J., & Colella, P. 1989, J. Comput. Phys., 82, 64
Bruenn, S. W. 1993, in Nuclear Physics in the Universe, ed. M. W. Guidry, & M. R. Strayer (Bristol: IOP), 31
Burrows, A., & Fryxell, B. A. 1993, ApJ, 418, L33
Burrows, A., Hayes, J., & Fryxell, B. A. 1995, ApJ, 450, 830
Chevalier, R. A. 1976, ApJ, 207, 872
Colella, P., & Glaz, H. M. 1985, J. Comput. Phys., 59, 264
Colella, P., & Woodward, P. R. 1984, J. Comput. Phys., 54, 174
Drake, R. P., Robey, H. F., Hurricane, O. A., et al. 2002, ApJ, 564, 896
Einfeldt, B. 1988, SIAM J. Num. Anal., 25, 294
Fassia, A., Meikle, W. P. S., Geballe, T. R., et al. 1998, MNRAS, 299, 150
Fesen, R. A., & Becker, R. H. 1991, ApJ, 371, 621
Filippenko, A. V., & Sargent, W. L. W. 1989, ApJ, 345, L43
Fishbine, B. 2002, Los Alamos Res. Quart., 3, 6
Fryxell, B., Müller, E., & Arnett, W. D. 1991, ApJ, 367, 619
Hachisu, I., Matsuda, T., Nomoto, K. I., & Shigeyama, T. 1990, ApJ, 358, L57
Hachisu, I., Matsuda, T., Nomoto, K. I., & Shigeyama, T. 1991, ApJ, 368, L27
Hachisu, I., Matsuda, T., Nomoto, K. I., & Shigeyama, T. 1992, ApJ, 390, 230
Hachisu, I., Matsuda, T., Nomoto, K. I., & Shigeyama, T. 1994, A&AS, 104, 341
Hamuy, M. 2003, ApJ, 582, 905
Harkness, R. P., Wheeler, J. C., Margon, B., et al. 1987, ApJ, 317, 355
Herant, M., & Benz, W. 1991, ApJ, 370, L81
Herant, M., & Benz, W. 1992, ApJ, 387, 294
Herant, M., Benz, W., & Colgate, S. 1992, ApJ, 395, 642
Herant, M., Benz, W., Hix, W. R., Fryer, C. L., & Colgate, S. A. 1994, ApJ, 435, 339
Herant, M., & Woosley, S. E. 1994, ApJ, 425, 814
Hillebrandt, W., & Höflich, P. 1989, Rep. Prog. Phys., 52, 1421
Hungerford, A. L., Fryer, C. L., & Warren, M. S. 2003, ApJ, submitted
Ivanova, N., Podsiadlowski, P., & Spruit, H. 2002, MNRAS, 334, 819
Iwamoto, K., Young, T. R., Nakasato, N., et al. 1997, ApJ, 477, 865
Janka, H.-T., Buras, R., Kifonidis, K., Plewa, T., & Rampp, M. 2003, in From Twilight to Highlight: The Physics of Supernovae, ed. W. Hillebrandt, & B. Leibundgut (Berlin: Springer)

Janka, H.-T., Kifonidis, K., & Rampp, M. 2001, in LNP 578: Physics of Neutron Star Interiors, ed. D. Blaschke, N. Glendenning, & A. Sedrakian (Berlin: Springer), 333
Janka, H.-T., & Müller, E. 1996, A&A, 306, 167
Kane, J., Arnett, W. D., Remington, B. A., et al. 2000, ApJ, 528, 989
Kane, J. O., Robey, H. F., Remington, B. A., et al. 2001, Phys. Rev. E, 63, 55 401
Keil, W., Janka, H.-T., & Müller, E. 1996, ApJ, 473, L111
Khokhlov, A. M., Höflich, P. A., Oran, E. S., et al. 1999, ApJ, 524, L107
Kifonidis, K., Plewa, T., Janka, H.-T., & Müller, E. 2000, ApJ, 531, L123
Kifonidis, K., Plewa, T., & Müller, E. 2001, in AIP Conf. Proc. 561: Tours Symp. on Nuclear Physics IV, ed. M. Arnould, M. Lewitowicz, Y. T. Oganessian, et al. (Melville, New York: American Institute of Physics), 21
Klein, R. I., Budil, K. S., Perry, T. S., & Bach, D. R. 2003, ApJ, 583, 245
Klein, R. I., McKee, C. F., & Colella, P. 1994, ApJ, 420, 213
LeVeque, R. J. 1998, in Computational Methods for Astrophysical Fluid Flow, ed. O. Steiner, & A. Gautschy (Berlin: Springer), 1
Liou, M.-S. 2000, J. Comput. Phys., 160, 623
Lucy, L. 1991, ApJ, 383, 308
McCray, R. 1993, ARA&A, 31, 175
Mezzacappa, A., Calder, A. C., Bruenn, S. W., et al. 1998, ApJ, 495, 911
Miller, D. S., Wilson, J. R., & Mayle, R. W. 1993, ApJ, 415, 278
Mitchell, R. C., Baron, E., Branch, D., et al. 2001, ApJ, 556, 979
Müller, E. 1998, in Computational Methods for Astrophysical Fluid Flow, ed. O. Steiner, & A. Gautschy (Berlin: Springer), 371
Müller, E., Fryxell, B., & Arnett, W. D. 1991a, in Supernova 1987 A and Other Supernovae, ed. J. Danziger, & K. Kjär (Garching: European Southern Observatory), 99
Müller, E., Fryxell, B., & Arnett, W. D. 1991b, A&A, 251, 505
Müller, E., Fryxell, B., & Arnett, W. D. 1991c, in Elba Workshop on Chemical and Dynamical Evolution of Galaxies, ed. F. Federini, J. Franco, & F. Matteucci (Pisa: ETS Editrice), 394
Müller, E., & Steinmetz, M. 1995, Comput. Phys. Commun., 89, 45
Nagataki, S., Hashimoto, M.-A., Sato, K., & Yamada, S. 1997, ApJ, 486, 1026
Nagataki, S., Shimizu, T. M., & Sato, K. 1998, ApJ, 495, 413
Nomoto, K. I., Shigeyama, T., Kumagai, S., & Hashimoto, M.-A. 1988, Proc. Astron. Soc. Austr., 7, 490
Nomoto, K. I., Shigeyama, T., Kumagai, S., Yamaoka, H., & Suzuki, T. 1994, in Supernovae, Les Houches Session LIV, ed. S. A. Bludman, R. Mochkovitch, & J. Zinn-Justin (Amsterdam: Elsevier/North-Holland)
Plewa, T., & Müller, E. 1999, A&A, 342, 179
Plewa, T., & Müller, E. 2001, Comput. Phys. Commun., 138, 101
Podsiadlowski, P. 1992, PASP, 104, 717
Quirk, J. J. 1994, Int. J. Num. Meth. Fluids, 18, 555
Quirk, J. J. 1997, in Upwind and High-Resolution Schemes, ed. M. Yousuff Hussaini, B. van Leer, & J. van Rosendale (Berlin: Springer), 550
Rampp, M., & Janka, H.-T. 2002, A&A, 396, 361
Robey, H. F., Kane, J. O., Remington, B. A., et al. 2001, Phys. Plasmas, 8, 2446
Sedov, L. I. 1959, Similarity and dimensional methods in mechanics (London: Infosearch)
Shigeyama, T., Iwamoto, K., Hachisu, I., Nomoto, K. I., & Saio, H. 1996, in Supernovae and supernova remnants, Proc. of the International Astronomical Union Coll. 145, ed. R. McCray, & Z. Wang (Cambridge, UK: Cambridge University Press), 129
Shigeyama, T., Nomoto, K. I., Tsujimoto, T., & Hashimoto, M.-A. 1990, ApJ, 361, L23
Spyromilio, J. 1991, MNRAS, 253, 25P
Spyromilio, J. 1994, MNRAS, 266, L61
Stone, J. M., & Norman, M. L. 1992, ApJ, 390, L17
Swartz, D. A., Filippenko, A. V., Nomoto, K. I., & Wheeler, J. C. 1993, ApJ, 411, 313
Thielemann, F.-K., Nomoto, K. I., & Hashimoto, M. 1996, ApJ, 460, 408
Thorstensen, J. R., Fesen, R. A., & van den Bergh, S. 2001, AJ, 122, 297
van den Bergh, S. 1971, ApJ, 165, 457
van Riper, K. A. 1979, ApJ, 232, 558
Wang, L., & Hu, J. 1994, Nature, 369, 380
Wang, L., Wheeler, J. C., Höflich, P., et al. 2002, ApJ, 579, 671
Wheeler, J. C., Meier, D. L., & Wilson, J. R. 2002, ApJ, 568, 807
Witti, J., Janka, H.-T., & Takahashi, K. 1994, A&A, 286, 841
Wooden, D. H. 1997, in Astrophysical Implications of the Laboratory Study of Presolar Materials, ed. T. J. Bernatowicz, & E. Zinner (Woodbury: American Institute of Physics), 317
Woosley, S. E., & Eastman, R. 1997, in Thermonuclear Supernovae, ed. P. Ruiz-LaPuente, R. Canal, & J. Isern (Dordrecht: Kluwer), 821
Woosley, S. E., Eastman, R. G., Weaver, T. A., & Pinto, P. A. 1994, ApJ, 429, 300
Woosley, S. E., Heger, A., Weaver, T. A., & Langer, N. 1997, MPA Preprint, 1024
Woosley, S. E., Langer, N., & Weaver, T. A. 1995, ApJ, 448, 315
Woosley, S. E., Pinto, P. A., & Ensman, L. 1988, ApJ, 324, 466
Woosley, S. E., & Weaver, T. A. 1995, ApJS, 101, 181
Yamada, S., & Sato, K. 1990, ApJ, 358, L9
Yamada, S., & Sato, K. 1991, ApJ, 382, 594
Zoldi, C. 2002, Ph.D. Thesis, State University of New York at Stony Brook